

Multipole analysis of pion photoproduction based on fixed t dispersion relations and unitarity

O. Hanstein, D. Drechsel and L. Tiator

Institut für Kernphysik, Universität Mainz, 55099 Mainz, Germany

(April 17, 2018)

We have analysed pion photoproduction imposing constraints from fixed t dispersion relations and unitarity. Coupled integral equations for the S and P wave multipoles were derived from the dispersion relations and solved by the method of Omnès and Muskhelishvili. The free parameters were determined by a fit to the most recent data for π^+ and π^0 production on the proton as well as π^- production on the neutron, in the energy range $160 \text{ MeV} \leq E_\gamma \leq 420 \text{ MeV}$. The lack of high precision data on the neutron and of polarization observables leads to some limitations of our results. Especially the multipole M_{1-} connected with the Roper resonance $P_{11}(1440)$ cannot be determined to the required precision. Our predictions for the threshold amplitudes are in good agreement with both the data and chiral perturbation theory. In the region of the $\Delta(1232)$ we have determined the ratio of electric quadrupole and magnetic dipole excitation. The position of the resonance pole is obtained in excellent agreement with pion-nucleon scattering, and the complex residues of the multipoles are determined with the speed-plot technique.

PACS numbers: 13.60.Le, 14.20.Gk, 11.55.Fv, 11.80.Et

Keywords: Pion photoproduction, dispersion relations, partial-wave analysis

I. INTRODUCTION

Pion photoproduction was extensively studied both theoretically and experimentally in the sixties and seventies. The basic theoretical approach was given by dispersion theory, especially by fixed t dispersion relations. Since perturbative methods of quantum field theory fail in the case of the strong interactions in the resonance region, dispersion relations seemed to be the only possible tool to treat hadronic processes on a quantitative level. Given the technical possibilities of that time, the statistics of the data was moderate and systematical errors were large. With the development of quantum chromodynamics (QCD) as a fundamental field theory in terms of quarks and gluons, the theoretical understanding of strong interactions has improved at the higher energies. However our understanding of hadron physics in the nonperturbative region at energies of the order of 1 GeV remains still unsatisfactory. Although quark models of different kinds give some description of the baryon and meson spectra, their predictive power for reactions is still quite poor. The only approach to infer all the symmetries of QCD into the physics at these energies is given by chiral perturbation theory (ChPT). However, the results of ChPT can be applied only in the threshold region. Recently, it has been investigated how to include the most prominent resonance of the nucleon, the $\Delta(1232)$, within the framework of heavy baryon ChPT. However, the first results achieved by this technique are not yet satisfactory. On the other side modern electron accelerators have provided a host of high precision data in the 90's, and will continue to do so. Beams of high current and high duty factor together with considerably improved particle detection techniques have reduced the statistical errors to the order of a few percent, and promise to keep control of the systematical errors at the same level. To interpret these data with respect to the most interesting features, i.e. the threshold behaviour and the electromagnetic excitation of resonances, a partial wave analysis is mandatory. To ensure the consistency and uniqueness of such an analysis, constraints from unitarity and dispersion relations have to be imposed. Such concepts have proven to be quite successful in pion-nucleon scattering [1]. In comparison with that field, the situation in pion photoproduction is considerably more complex. The spin and isospin structure leads to twelve independent amplitudes, while in pion-nucleon scattering there are only four such amplitudes. As a consequence a complete experiment [2] requires the use of many polarization observables. Such a complete experiment has not yet been performed. However, the new experiments provide an ever increasing amount of precise and new data. At present, the experimental thrust is mainly on measurements near threshold and around the $\Delta(1232)$ resonance. In the coming years, a series of experiments at Jefferson Lab will cover the whole resonance region. Restricting our theoretical investigations to the threshold region and the low-lying resonances, we are lead to choose the method of Omnès and Muskhelishvili to analyse the existing data, because it introduces a natural parametrization and fulfills the constraints of unitarity at the same trace.

In the future, the required shift to include also higher energies will make it necessary to take account of the full content of dispersion methods and to apply more involved techniques. At the moment, however, we obtain an excellent representation of the analysed data by use of the method of Ref. [3]. Therefore we deem it worthwhile extending this

method to the second resonance region as a next step.

In Sec. 2 of this contribution we briefly recall the kinematics, amplitudes and (polarization) observables of pion photoproduction. The essential ingredients of dispersion relations at fixed t are outlined in Sec. 3. The method of Omnès and Muskhelishvili to solve these coupled integral equations is given in Sec. 4. In particular, we also discuss our choice of the free parameters of that method, which are then fitted to our data basis (Sec. 5). This fit defines the result for the multipole amplitudes, which are presented in Sec. 6. In particular we give our prediction for the threshold production of charged and neutral pions, the ratio of electric quadrupole and magnetic dipole radiation in the region of the $\Delta(1232)$, and the inclusive cross sections. We conclude with a short summary and outlook in Sec. 7.

II. FORMALISM

A. Kinematics and conventions

The four-momenta occurring in the reaction are denoted by $q = (\omega, \vec{q})$ for the photon, $k = (\omega_\pi, \vec{k})$ for the pion, $P_i = (P_i^0, \vec{P}_i)$ and $P_f = (P_f^0, \vec{P}_f)$ for the nucleon in the initial and the final state, respectively. With this notation the conventional Mandelstam variables are

$$s = (P_i + q)^2 = (P_f + k)^2 = W^2, \quad (1)$$

$$t = (k - q)^2 = (P_f - P_i)^2, \quad (2)$$

$$u = (P_f - q)^2 = (P_i - k)^2, \quad (3)$$

where W is the cm energy. Since all calculations are performed in the cm frame, we further introduce the cm energy of the nucleons,

$$E_{i,f} = P_{i,f}^{0,cm}. \quad (4)$$

In the following we will suppress the index cm for the momenta,

$$\vec{q} = \vec{q}^{cm} = -\vec{P}_i^{cm}, \quad (5)$$

$$\vec{k} = \vec{k}^{cm} = -\vec{P}_f^{cm}, \quad (6)$$

and introduce the quantity $x = \cos \theta$ instead of the scattering angle $\theta = \theta^{cm}$. In the discussion of our results for the amplitudes and observables, the photon energy is usually given in the lab frame, $E_\gamma = E_\gamma^{lab}$.

B. Amplitudes

The invariant amplitudes $A_i(s, t, u)$ are defined according to [4]. The relativistic invariants are¹

$$M_1 = i\gamma_5 \not{\epsilon} \not{q}, \quad (7)$$

$$M_2 = 2i\gamma_5 (P \cdot q \not{k} \cdot \epsilon - P \cdot \epsilon \not{k} \cdot q), \quad (8)$$

$$M_3 = i\gamma_5 (\not{\epsilon} \not{k} \cdot q - \not{q} \not{k} \cdot \epsilon), \quad (9)$$

$$M_4 = 2i\gamma_5 (\not{\epsilon} P \cdot q - \not{q} P \cdot \epsilon - m_N \not{\epsilon} \not{q}), \quad (10)$$

where ϵ is the polarization vector of the photon and $P = \frac{1}{2}(P_i + P_f)$. The scattering operator T , to be evaluated between the Dirac spinors of the nucleon, is expressed in terms of the invariants by

$$T = \sum_{i=1}^4 A_i(s, t, u) M_i. \quad (11)$$

The photoproduction amplitudes A_i can be decomposed in isospace according to

¹For the metric and the γ matrices we adopt the conventions of Ref. [5].

$$A_i = \frac{1}{2}A_i^{(-)}[\tau_\alpha, \tau_0] + A_i^{(+)}\delta_{\alpha 0} + A_i^{(0)}\tau_\alpha, \quad (12)$$

with the Pauli matrices τ_α acting on the isospinor of the nucleon. The behaviour of the invariant amplitudes under crossing is

$$A_k^I(s, t, u) = \varepsilon^I \xi_k A_k^I(u, t, s), \quad (13)$$

$$I = +, 0, -; \quad \xi_1 = \xi_2 = -\xi_3 = \xi_4 = 1; \quad \varepsilon^+ = \varepsilon^0 = -\varepsilon^- = 1.$$

The physical amplitudes may be expressed by the isospin combinations

$$A(\gamma p \rightarrow n\pi^+) = \sqrt{2}(A^{(-)} + A^{(0)}) = \sqrt{2}({}_p A^{(\frac{1}{2})} - \frac{1}{3}A^{(\frac{3}{2})}), \quad (14)$$

$$A(\gamma p \rightarrow p\pi^0) = A^{(+)} + A^{(0)} = {}_p A^{(\frac{1}{2})} + \frac{2}{3}A^{(\frac{3}{2})}, \quad (15)$$

$$A(\gamma n \rightarrow p\pi^-) = -\sqrt{2}(A^{(-)} - A^{(0)}) = \sqrt{2}({}_n A^{(\frac{1}{2})} + \frac{1}{3}A^{(\frac{3}{2})}), \quad (16)$$

$$A(\gamma n \rightarrow n\pi^0) = A^{(+)} - A^{(0)} = -{}_n A^{(\frac{1}{2})} + \frac{2}{3}A^{(\frac{3}{2})}. \quad (17)$$

The amplitudes $A^{(\frac{1}{2})}$ and $A^{(\frac{3}{2})}$ refer to final states of definite isospin ($\frac{1}{2}$ or $\frac{3}{2}$). They are combinations of the quantities $A^{(+)}$ and $A^{(-)}$ of Eq. (12),

$$A^{(\frac{1}{2})} = A^{(+)} + 2A^{(-)}, \quad A^{(\frac{3}{2})} = A^{(+)} - A^{(-)}. \quad (18)$$

For the isospin $\frac{1}{2}$ channel it is also useful to define the combinations

$${}_p A^{(\frac{1}{2})} = A^{(0)} + \frac{1}{3}A^{(\frac{1}{2})}, \quad {}_n A^{(\frac{1}{2})} = A^{(0)} - \frac{1}{3}A^{(\frac{1}{2})}, \quad (19)$$

which enter into the amplitudes of the reactions on the proton or the neutron, respectively.

Evaluating Eq. (11) between the nucleon Dirac spinors in the cm frame, expressing the result by Pauli spinors and multiplying by a factor $m_N/4\pi W$, we obtain the form [4]

$$\mathcal{F} = i\vec{\sigma} \cdot \vec{\varepsilon} \mathcal{F}_1 + \vec{\sigma} \cdot \hat{k} \vec{\sigma} \cdot (\hat{q} \times \vec{\varepsilon}) \mathcal{F}_2 + i\vec{\sigma} \cdot \hat{q} \hat{k} \cdot \vec{\varepsilon} \mathcal{F}_3 + i\vec{\sigma} \cdot \hat{k} \hat{k} \cdot \vec{\varepsilon} \mathcal{F}_4, \quad (20)$$

where \hat{q} and \hat{k} are unit vectors in the direction of the respective momenta. The cm differential cross section can be expressed through the CGLN amplitudes \mathcal{F}_i defined by Eq. (20),

$$\frac{d\sigma}{d\Omega} = \frac{|\vec{k}|}{|\vec{q}|} |\chi_f^\dagger \mathcal{F} \chi_i|^2, \quad (21)$$

where $\chi_{f,i}$ are nucleon spinors. The connection between the CGLN amplitudes and the invariant amplitudes is given by

$$\begin{aligned} F_1 &= 4\pi \frac{2W}{(W - m_N)} \frac{\mathcal{F}_1}{[(E_f + m_N)(E_i + m_N)]^{\frac{1}{2}}} \\ &= A_1 + (W - m_N)A_4 - \frac{t - m_\pi^2}{2(W - m_N)}(A_3 - A_4), \\ F_2 &= 4\pi \frac{2W}{(W - m_N)} \left(\frac{E_f + m_N}{E_i + m_N} \right)^{\frac{1}{2}} \frac{\mathcal{F}_2}{|\vec{k}|} \\ &= -A_1 + (W + m_N)A_4 - \frac{t - m_\pi^2}{2(W + m_N)}(A_3 - A_4), \\ F_3 &= 4\pi \frac{2W}{(W - m_N)} \frac{\mathcal{F}_3}{[(E_f + m_N)(E_i + m_N)]^{\frac{1}{2}} |\vec{k}|} \\ &= (W - m_N)A_2 + (A_3 - A_4), \\ F_4 &= 4\pi \frac{2W}{(W - m_N)} \left(\frac{E_f + m_N}{E_i + m_N} \right)^{\frac{1}{2}} \frac{\mathcal{F}_4}{|\vec{k}|^2} \\ &= -(W + m_N)A_2 + (A_3 - A_4). \end{aligned} \quad (22)$$

For practical calculations it is useful to introduce a matrix form for the different amplitudes,

$$\vec{\mathcal{F}} = \mathbf{H}\vec{F}, \quad \vec{F} = \mathbf{C}\vec{A}, \quad \vec{A} = \mathbf{C}^{-1}\vec{F}, \quad (23)$$

where \vec{A} , $\vec{\mathcal{F}}$ and \vec{F} are vectors with the four elements defined in Eqs. (11), (20) and (22) respectively. The 4×4 matrices \mathbf{C} and \mathbf{H} contain kinematical factors only and are given in appendix A.

The CGLN amplitudes are expanded into the multipoles $E_{l\pm}$ and $M_{l\pm}$ which conserve parity and total angular momentum J ,

$$\begin{aligned} \mathcal{F}_1(W, \theta) &= \sum_{l \geq 0} \{ (lM_{l+}(W) + E_{l+}(W))P'_{l+1}(x) \\ &\quad + [(l+1)M_{l-}(W) + E_{l-}(W)]P'_{l-1}(x) \}, \\ \mathcal{F}_2(W, \theta) &= \sum_{l \geq 1} [(l+1)M_{l+}(W) + lM_{l-}(W)]P'_l(x), \\ \mathcal{F}_3(W, \theta) &= \sum_{l \geq 1} [(E_{l+}(W) - M_{l+}(W))P''_{l+1}(x) \\ &\quad + (E_{l-}(W) + M_{l-}(W))P''_{l-1}(x)], \\ \mathcal{F}_4(W, \theta) &= \sum_{l \geq 2} (M_{l+}(W) - E_{l+}(W) - M_{l-}(W) - E_{l-}(W))P'_l(x). \end{aligned} \quad (24)$$

E and M denote the electric or magnetic character of the incoming photon, the indices $l\pm$ describe the coupling of the pion angular momentum l and the nucleon spin to the total angular momentum $J = l \pm \frac{1}{2}$.

The 4 partial waves with angular momentum l may be written in terms of a vector,

$$\vec{\mathcal{M}}_l(W)^T = (E_{l+}(W), E_{l-}(W), M_{l+}(W), M_{l-}(W)), \quad (25)$$

where T stands for transposed. The matrix form of the multipole expansion Eq. (24) and its inverse read

$$\vec{\mathcal{F}}(W, x) = \sum_{l=0}^{\infty} \mathbf{G}_l(x) \vec{\mathcal{M}}_l(W), \quad (26)$$

$$\vec{\mathcal{M}}_l(W) = \int_{-1}^1 dx \mathbf{D}_l(x) \vec{\mathcal{F}}(W, x), \quad (27)$$

with the 4×4 matrices \mathbf{G}_l and \mathbf{D}_l given in appendix A.

The multipole amplitudes $\mathcal{M}_{l\pm}$ are complex functions of the cm energy W . Below inelastic threshold, the Fermi-Watson theorem [6] allows one to express the complex phases of the multipoles by the corresponding pion-nucleon scattering phase shifts,

$$\mathcal{M}_{l\pm}^I(W) = |\mathcal{M}_{l\pm}^I(W)| e^{i(\delta_{l\pm}^I(W) + n\pi)}, \quad (28)$$

with $I = \frac{1}{2}, \frac{3}{2}$.

C. Observables

If polarization degrees of freedom are taken into account, the differential cross section of pion photoproduction takes the form [7]

$$\begin{aligned} \frac{d\sigma}{d\Omega} &= \frac{|\vec{k}|}{|\vec{q}|} \{ (R_T + P_{n_{i,f}} R_T^{n_{i,f}}) + \Pi_T [(R_{TT} + P_{n_{i,f}} R_{TT}^{n_{i,f}}) \cos 2\varphi \\ &\quad - (P_{i,f} R_{TT}^{l_{i,f}} + P_{t_{i,f}} R_{TT}^{t_{i,f}}) \sin 2\varphi] + \Pi_C (P_{i,f} R_{TT'}^{l_{i,f}} + P_{t_{i,f}} R_{TT'}^{t_{i,f}}) \}. \end{aligned} \quad (29)$$

The various response functions R may be expressed through the CGLN amplitudes. P_i are the components of the nucleon polarization vector, Π_T is the degree of linear polarization of the photon, φ the angle between the reaction plane and the photon polarization, and Π_C the degree of circular photon polarization. The observables containing the information of the various polarization measurements are the appropriate asymmetries. In the following we will restrict the discussion to single polarization observables only. The beam asymmetry Σ which is measured with linearly polarized photons, perpendicular and parallel to the production plane is

$$\Sigma = \frac{d\sigma^\perp - d\sigma^\parallel}{d\sigma^\perp + d\sigma^\parallel} = \frac{-R_{TT}}{R_T}. \quad (30)$$

The target asymmetry T and the recoil polarization P ,

$$T = \frac{d\sigma^{P_{n_i}=1} - d\sigma^{P_{n_i}=-1}}{d\sigma^{P_{n_i}=1} + d\sigma^{P_{n_i}=-1}} = \frac{R_T^{n_i}}{R_T}, \quad (31)$$

$$P = \frac{d\sigma^{P_{n_f}=1} - d\sigma^{P_{n_f}=-1}}{d\sigma^{P_{n_f}=1} + d\sigma^{P_{n_f}=-1}} = \frac{R_T^{n_f}}{R_T}, \quad (32)$$

are determined with respect to the polarization of the incoming (outgoing) nucleon perpendicular to the production plane. In appendix B the relevant response functions are given as functions of the CGLN amplitudes.

III. DISPERSION RELATIONS AT FIXED t

The starting point of our analysis are dispersion relations at fixed t for the invariant amplitudes [8],

$$\text{Re}A_k^I(s, t) = A_k^{I,\text{pole}}(s, t) + \frac{1}{\pi} \mathcal{P} \int_{s_{\text{thr}}}^{\infty} ds' \left(\frac{1}{s' - s} + \frac{\varepsilon^I \xi_k}{s' - u} \right) \text{Im}A_k^I(s', t), \quad (33)$$

with $I = 0, \pm$ and $s_{\text{thr}} = (m_N + m_\pi)^2$. The pole term contributions $A_k^{I,\text{pole}}$ can be obtained by evaluating the Born approximation in pseudoscalar coupling,

$$\begin{aligned} A_1^{I,\text{pole}}(s, t) &= \frac{eg}{2} \left(\frac{1}{s - m_N^2} + \frac{\varepsilon^I}{u - m_N^2} \right), \\ A_2^{I,\text{pole}}(s, t) &= -\frac{eg}{t - m_\pi^2} \left(\frac{1}{s - m_N^2} + \frac{\varepsilon^I}{u - m_N^2} \right) = \frac{eg}{s - m_N^2} \left(\frac{\varepsilon^I - 1}{t - m_\pi^2} + \frac{\varepsilon^I}{u - m_N^2} \right), \\ A_3^{I,\text{pole}}(s, t) &= -\frac{eg}{2m_N} \frac{\kappa^I}{2} \left(\frac{1}{s - m_N^2} - \frac{\varepsilon^I}{u - m_N^2} \right), \\ A_4^{I,\text{pole}}(s, t) &= -\frac{eg}{2m_N} \frac{\kappa^I}{2} \left(\frac{1}{s - m_N^2} + \frac{\varepsilon^I}{u - m_N^2} \right), \end{aligned} \quad (34)$$

with $\kappa^{(+,-)} = \kappa_p - \kappa_n$ and $\kappa^{(0)} = \kappa_p + \kappa_n$, where κ_p and κ_n are the anomalous magnetic moments of the proton and the neutron, respectively. For the pion nucleon coupling constant g we take the value $g^2/4\pi = 14.28$ [1].

The next step is to apply the multipole projection to the dispersion relations (33). With the help of Eqs. (23) we obtain

$$\text{Re}\mathbf{F}^I(W, x) = \mathbf{F}^{I,\text{pole}}(W, x) + \frac{1}{\pi} \mathcal{P} \int_{W_{\text{thr}}}^{\infty} dW' \mathbf{E}^I(W, W', x') \text{Im}\mathbf{F}^I(W', x'), \quad (35)$$

where $x' = \cos \theta'$ corresponds to W' at fixed t . With

$$t - m_\pi^2 = -2\omega\omega_\pi + 2|\vec{k}||\vec{q}| \quad x = -2\omega'\omega'_\pi + 2|\vec{k}'||\vec{q}'| \quad x' \quad (36)$$

we have

$$x' = ex + f; \quad e = \frac{|\vec{k}||\vec{q}|}{|\vec{k}'||\vec{q}'|}; \quad f = \frac{-\omega\omega_\pi + \omega'\omega'_\pi}{|\vec{k}'||\vec{q}'|}. \quad (37)$$

The entries of the matrix $\mathbf{E}^I(W, W', x')$ are given in appendix A. Application of Eqs. (26) and (27) leads to a system of coupled integral equations for the multipole amplitudes,

$$\text{Re}\mathcal{M}_l^I(W) = \mathcal{M}_l^{I,\text{pole}}(W) + \frac{1}{\pi}\mathcal{P} \int_{W_{\text{thr}}}^{\infty} dW' \sum_{l'=0}^{\infty} \mathcal{K}_{ll'}^I(W, W') \text{Im}\mathcal{M}_l^I(W'). \quad (38)$$

The integral kernels

$$\mathcal{K}_{ll'}^I(W, W') = \int_{-1}^1 dx \mathbf{D}_l(x) \mathbf{H}(W) \mathbf{E}^I(W, W', x') \mathbf{H}^{-1}(W') \mathbf{G}_{l'}(x') \quad (39)$$

couple the multipoles with each other. Analytic expressions of these kernels have been given in Refs. [9,10] for the S and P waves. These kernels are regular kinematical functions except for the diagonal kernels \mathcal{K}_{ll}^I , which contain a term $\propto 1/(W - W')$. Our further analysis is based on Eqs. (38), which may be solved by several methods. In [9] conformal mapping techniques have been used. The work of Schwela and Weizel [3] follows the method of Omnès [11]. Lebedev [12] uses Padé approximants. Since our aim is to analyse new experimental data and not to give mere predictions, we essentially follow the work of [3] leading to a natural parametrization of the multipoles. Before we turn to this point in the next section, we have to make some remarks.

The dispersion relations (33) are valid for the isospin components with $I = \pm, 0$. Since the unitarity condition (28) will be imposed on the solutions for the multipoles, we have to work with amplitudes of definite isospin $\frac{1}{2}$ or $\frac{3}{2}$. This leads to a mixing of the components with $I = +$ and $I = -$. The corresponding linear combinations of the integral kernels are obtained as follows. If the kernel connecting the multipoles $\mathcal{M}_{l'}^{I'}$ and \mathcal{M}_l^I ($I = 0, \frac{1}{2}, \frac{3}{2}$ in the following) is denoted by $\mathcal{K}_{ll'}^{II'}$, Eqs. (18) lead to the relations

$$\begin{aligned} I' = \frac{3}{2} : \quad \mathcal{K}_{ll'}^{II'} &= \frac{1}{3} (2c_+^I \mathcal{K}_{ll'}^+ - c_-^I \mathcal{K}_{ll'}^-), \\ I' = \frac{1}{2} : \quad \mathcal{K}_{ll'}^{II'} &= \frac{1}{3} (c_+^I \mathcal{K}_{ll'}^+ + c_-^I \mathcal{K}_{ll'}^-), \\ I' = 0 : \quad \mathcal{K}_{ll'}^{II'} &= c_0^I \mathcal{K}_{ll'}^0, \end{aligned} \quad (40)$$

with $c_+^{3/2} = c_+^{1/2} = c_0^0 = 1$, $c_-^{3/2} = -1$, $c_-^{1/2} = 2$ and all other coefficients vanishing.

In this work we restrict ourselves to the energy region up to $E_\gamma \approx 500$ MeV. The first reason for this are possible problems with the convergence of the partial wave expansion which might occur in the unphysical region, when the path of the dispersion integrals leads outside of the Lehmann ellipses [13]. Furthermore, in this energy region it is reasonable to restrict the solution of the integral equations to S , P and eventually D waves. At energies near the second resonance region, higher partial waves have to be taken into account which will considerably complicate the procedure. Finally our method provides the most reliable results as long as the complex phases of the partial waves are known. This is the case below two-pion threshold. Nevertheless it can be assumed that the effects of inelasticities remain small also at somewhat higher energies. As a consequence of these restrictions, our results will be especially useful for the study of low energy amplitudes and the electromagnetic excitation of the $\Delta(1232)$.

IV. SOLUTION OF THE INTEGRAL EQUATIONS

On condition that the complex phases of the solutions are known, Omnès [11] has proposed to solve the integral equations (38) as follows. Introducing the functions

$$h_l^I(W) = e^{i\phi_l^I(W)} \sin \phi_l^I(W), \quad (41)$$

with the complex phase $\phi_l^I(W)$ of the multipole \mathcal{M}_l^I , one obtains

$$\text{Im}\mathcal{M}_l^I(W) = h_l^{I*}(W) \mathcal{M}_l^I(W). \quad (42)$$

Next one defines the amplitudes

$$M_l^I(W) = r_l(W) \mathcal{M}_l^I \quad (43)$$

by taking out kinematical factors for the S and P wave amplitudes,

$$\begin{aligned} r_{0+} &= \frac{W}{D_i D_f (W - m_N)}, \\ r_{1-} &= \frac{W D_f}{|\vec{k}| (W - m_N) D_i}, \\ r_{1+}(W) &= \frac{W}{D_i D_f (W - m_N) |\vec{k}| |\vec{q}|}, \end{aligned} \quad (44)$$

with $D_{i,f} = \sqrt{E_{i,f} + m_N}$. The coupled system of integral equations is now cast into the form

$$\begin{aligned} M_l^I(W) &= M_l^{I,\text{pole}}(W) + \frac{1}{\pi} \int_{W_{\text{thr}}}^{\infty} \frac{h_l^{I*}(W') M_l^I(W') dW'}{W' - W - i\varepsilon} \\ &+ \frac{1}{\pi} \sum_{l', I'} \int_{W_{\text{thr}}}^{\infty} K_{ll'}^{II'}(W, W') h_{l'}^{I'*}(W') M_{l'}^{I'}(W') dW', \end{aligned} \quad (45)$$

where the singular term has now been treated individually and subtracted from the integral kernel,

$$K_{ll'}^{II'}(W, W') = \frac{r_l(W)}{r_{l'}(W')} \mathcal{K}_{ll'}^{II'}(W, W') - \frac{\delta_{ll'} \delta_{II'}}{W' - W}. \quad (46)$$

In order to treat Eqs. (45), some further simplifications and assumptions are necessary. First of all, the infinite sum over l' has to be cut off. It can be shown that for multipoles with small complex phases in the relevant energy region, the solutions of the integral equations are essentially given by the inhomogeneities, i. e. the pole terms. Therefore we solve Eqs. (45) only for the S , P and D_{13} waves, and represent the higher partial waves by the inhomogeneities. A study of the integral kernels shows that many of them can be neglected. This leads to further simplifications.

To solve Eqs. (45) the complex phases $\phi_l^I(W)$ of the multipoles have to be known over the whole range of integration. From the Fermi-Watson theorem (28) we know that these phases are equal to the pion-nucleon scattering phase shifts below two-pion threshold. Above the inelastic threshold, $\phi_l^I(W)$ is no longer uniquely determined by unitarity. However it has been shown that the following ansatz for $\phi_l^I(W)$ can be motivated from the unitarity relation of the inelastic amplitudes [3],

$$\phi_l^I(W) = \arctan \left(\frac{1 - \eta_l^I(W) \cos 2\delta_l^I(W)}{\eta_l^I(W) \sin 2\delta_l^I(W)} \right). \quad (47)$$

Below two-pion threshold the ansatz (47) leads to the πN scattering phase shifts δ_l^I . Above this threshold the inelasticity parameters η_l^I as determined from pion-nucleon scattering enter into the formula. The ansatz (47) is justified if both $\gamma N \rightarrow n\pi N$ and $\pi N \rightarrow n\pi N$ are dominated by the same resonant intermediate state or if both matrix elements are real (e.g. if they are both described by one particle exchange) or imaginary (e.g. in the case of purely diffractive processes). In the case of the P_{13} waves the ansatz (47) would lead to an unphysical resonant behaviour. Therefore in this case we choose the alternative ansatz

$$\phi_l^I(W) = \arctan \left(\frac{\eta_l^I(W) \sin 2\delta_l^I(W)}{1 + \eta_l^I(W) \cos 2\delta_l^I(W)} \right) \quad (48)$$

which has also been derived in Ref. [3].

At higher energies, where information from pion-nucleon scattering is no longer available, certain assumptions have to be made in order to interpolate the phases to infinity [3]. As an alternative we cut off the integrals of Eq. (45) at $W = 2$ GeV and represent the high energy tails of the dispersion integrals by t -channel exchange of ρ - and ω -mesons, leading to the contributions:

$$\begin{aligned}
A_1^V &= \frac{\lambda_V}{m_V} \frac{g_V^\mathcal{T}}{2m_N} \frac{t}{t - m_V^2}, & A_2^V &= -\frac{\lambda_V}{m_V} \frac{g_V^\mathcal{T}}{2m_N} \frac{1}{t - m_V^2}, \\
A_3^V &= 0, & A_4^V &= -\frac{\lambda_V}{m_V} g_V^\mathcal{V} \frac{1}{t - m_V^2},
\end{aligned} \tag{49}$$

where V stands for ω or ρ respectively, λ_V is taken from the radiative decay of the vector mesons and $g_V^{\mathcal{V},\mathcal{T}}$ are the vector and tensor couplings at the VNN vertex. The integral equations now take the form

$$\begin{aligned}
M_l^I(W) &= M_l^{I,\text{pole}}(W) + \frac{1}{\pi} \int_{w_{\text{thr}}}^\Lambda \frac{h_l^{I*}(W') M_l^I(W') dW'}{W' - W - i\varepsilon} \\
&+ \frac{1}{\pi} \sum_{l', I'} \int_{w_{\text{thr}}}^\Lambda K_{ll'}^{II'}(W, W') h_{l'}^{I'*}(W') M_{l'}^{I'}(W') dW' + M_l^{I,V}(W),
\end{aligned} \tag{50}$$

with a cut-off at $\Lambda = 2$ GeV. The high energy parametrization by t -channel exchange leads to a further inhomogeneity of the integral equations, $M_l^{I,V}(W)$, to be constructed according to the rules given above. In comparison with [11] this leads to a slight modification of the solutions. As in [11] we first solve the characteristic equations

$$\begin{aligned}
M_l^I(W) &= M_l^{I,\text{pole}}(W) + \frac{1}{\pi} \int_{w_{\text{thr}}}^\Lambda \frac{h_l^{I*}(W') M_l^I(W') dW'}{W' - W - i\varepsilon} \\
&+ M_l^{I,V}(W),
\end{aligned} \tag{51}$$

which contain only the singular part of the integral equations. The general solutions are

$$\begin{aligned}
M_l^I(W) &= M_l^{I,\text{pole}}(W) + M_l^{I,V}(W) \\
&+ \frac{M_{l,0}^{I,\text{hom}}(W)}{\pi} \int_{w_{\text{thr}}}^\Lambda \frac{h_l^I(W') (M_l^{I,\text{pole}}(W') + M_l^{I,V}(W')) dW'}{M_{l,0}^{I,\text{hom}}(W') (W' - W - i\varepsilon)} \\
&+ P(W) M_{l,0}^{I,\text{hom}}(W),
\end{aligned} \tag{52}$$

with

$$M_{l,0}^{I,\text{hom}}(W) = \exp \left\{ \frac{W}{\pi} \int_{w_{\text{thr}}}^\Lambda \frac{\phi_l^I(W') dW'}{W' (W' - W - i\varepsilon)} \right\} \tag{53}$$

a solution of the homogeneous equation

$$M_l^I(W) = \frac{1}{\pi} \int_{w_{\text{thr}}}^\Lambda \frac{h_l^{I*}(W') M_l^I(W') dW'}{W' - W - i\varepsilon}, \tag{54}$$

and $P(W)$ an arbitrary polynomial. In our calculations for this polynomial only the simplest case, i.e. a real constant, will occur.

If the self-coupling of $M_l^I(W)$ is fully taken into account, Eq. (50) has to be transformed into an equation of the Fredholm type,

$$M_l^I(W) = N_l^I(W) + \sum_{l', I'} \frac{1}{\pi} \int_{w_{\text{thr}}}^\Lambda F_{ll'}^{II'}(W, W') h_{l'}^{I'*}(W') M_{l'}^{I'}(W') dW', \tag{55}$$

with

$$N_l^I(W) = M_l^{I,\text{pole}}(W) + M_l^{I,V}(W) + \frac{M_{l,0}^{I,\text{hom}}(W)}{\pi} \int_{w_{\text{thr}}}^{\Lambda} \frac{h_l^I(W')(M_l^{I,\text{pole}}(W') + M_l^{I,V}(W'))dW'}{M_{l,0}^{I,\text{hom}}(W')(W' - W - i\varepsilon)} \quad (56)$$

and the Fredholm kernels

$$F_{ll'}^{II'}(W, W') = K_{ll'}^{II'}(W, W')h_l^{I'*}(W') + \frac{M_{l,0}^{I,\text{hom}}(W)}{\pi} \times \int_{w_{\text{thr}}}^{\Lambda} \frac{h_l^{I'}(W'')K_{ll'}^{II'}(W'', W')h_l^{I*}(W')dW''}{M_{l,0}^{I,\text{hom}}(W'')(W'' - W - i\varepsilon)}. \quad (57)$$

Eq. (55) can now be solved by standard numerical methods. We mention that also the solution of Eq. (55) is not unique. A solution of the corresponding homogeneous equation can be added in the same way as in the case of Eq. (51). For the mathematical details of solving the homogeneous equation see Ref. [10].

Numerically we found that the self-couplings of the multipoles are given to good approximation by the singular parts of the integral equations, except for the P_{33} multipoles $M_{1+}^{(\frac{3}{2})}$ and $E_{1+}^{(\frac{3}{2})}$. Therefore, the Fredholm equations have to be solved for these P -waves, while in all other cases it is quite sufficient to solve the characteristic equations. If the couplings to other multipoles are taken into account, they enter into the equations as further inhomogeneities. If we neglect all integral kernels giving only small contributions, we obtain the following procedure to solve the integral equations for the S -, P - and D_{13} -waves:

1. The amplitude $M_{1+}^{(\frac{3}{2})}$ is practically independent of the other multipoles. The corresponding Fredholm equation has to be solved.
2. Having solved the equation for $M_{1+}^{(\frac{3}{2})}$, we calculate its contribution to $E_{1+}^{(\frac{3}{2})}$ entering into the corresponding equation as a further inhomogeneity.
3. The equations for $M_{1-}^{(\frac{1}{2})}$ and $M_{1-}^{(\frac{3}{2})}$ are solved taking account of the influence of $M_{1+}^{(\frac{3}{2})}$ and $E_{1+}^{(\frac{3}{2})}$.
4. For $E_{0+}^{(\frac{1}{2})}$ and $E_{0+}^{(\frac{3}{2})}$ also the contributions of the M_{1-} components are important.
5. In the isospin 0 channel, only the contribution of $M_{1-}^{(0)}$ to $E_{0+}^{(0)}$ has to be taken into account.
6. For all other P waves as well as the D_{13} multipoles we only have to solve the characteristic equations.

According to Eq. (52) we can add to each solution of the inhomogeneous equation a solution of the homogeneous equation multiplied by an arbitrary polynomial in W . Following the arguments of [3], we restrict ourselves to the addition of homogeneous solutions to the multipoles $E_{0+}^{(0)}$, $E_{0+}^{(\frac{1}{2})}$, $M_{1-}^{(0)}$, $M_{1-}^{(\frac{1}{2})}$, $E_{1+}^{(\frac{3}{2})}$ and $M_{1+}^{(\frac{3}{2})}$ multiplied by a real constant. These six constants are determined by a fit to the data. Further parameters of our fit are the coupling constants of the vector mesons. In [3] it is argued that vector meson exchange should not be included because of double counting. This argument is correct because the authors evaluate the occurring integrals to infinity. From a study of unitarity diagrams it can be seen that the integrals in fact contain the vector meson contributions. In our case, however, the integrals run only to the cut off Λ , and only a fraction of vector meson exchange will be contained in the integrals. The remaining part is assumed to be the dominant contribution at the higher energies, which we represent by vector meson exchange as described with four free VNN coupling constants fitted to the data. Thus we end up with ten free parameters.

In solving the integral equations we have to know the scattering phase shifts and inelasticity parameters of pion nucleon scattering. They are taken from the SAID code (solution SM95 [14]).

V. THE FIT TO THE DATA

We have determined the ten free parameters of our approach by a fit to selected photoproduction data for $160 \text{ MeV} \leq E_\gamma \leq 420 \text{ MeV}$ (see Tab. I). Most interesting for our analysis are the new data from MAMI. Differential cross sections of π^0 production off the proton near threshold [15], and differential cross sections as well as beam asymmetries Σ for both π^+ and π^0 production off the proton [16,17] have been measured with high precision. Since there are no new low energy data for π^+ we include those of the data compilation [18]. We have also included the most recent data from ELSA, differential cross sections for π^+ production [19] and the target asymmetries T for π^+ and π^0 production off the proton [20]. To get the full isospin decomposition we also had to include data for π^- production, for which we took the differential cross sections given in Refs. [21–25]. Altogether we have included 1751 data points. The overall χ^2 per data point of 2.8. We note that we have not renormalized the different data sets in our fit.

In Figs. 1–12 we show our results for the observables. In general we obtain a good description of the photoproduction data. The differential cross sections and beam asymmetries for π^+ production are in perfect agreement with the Mainz experiment [16] except for the differential cross sections around 330 MeV where we find a slight discrepancy (see Fig. 3). In our local fit (see next section) this discrepancy could not be removed which means that there is a problem either with our parametrization or with the experiment. We stress that also at these energies the beam asymmetries, which are less sensitive to systematical errors, are well described by our fit (see Fig. 4). From the experimental point of view one main difficulty are measurements concerning π^+ production at very low energies. Because of the short life time of charged pions many of them decay before detection. As a consequence the existing data have large error bars. In Fig. 1 we show the result of the fit compared to the world data. We find good agreement within the statistical uncertainties. The differential cross sections and target asymmetries from Bonn which we included in our fit (see Figs. 2 and 5) have larger errors than the new Mainz data. In the case of the target asymmetries our result seems to be consistent with the data if the statistical uncertainty is taken into account, except for very low energies where the experimental values are systematically larger than our curves. However, it can be shown that such large values of T would require much larger imaginary parts of the partial waves than allowed by unitarity considerations.

In π^0 production on the proton we find a somewhat different situation. In this case the results of recent high precision experiments at low energies are available [15]. However, only the differential cross sections for $E_\gamma \geq 160 \text{ MeV}$ were included in our fit. The description is reasonably good also for the lower energies (see Fig. 6). At higher energies we again find a very nice description of the beam asymmetries (see Fig. 9). Also the differential cross sections are well described except for the energies around 330 MeV (see Figs. 7 and 8). The target asymmetries are only in semiquantitative agreement (see Fig. 10).

In pion production on the neutron the experimental situation is less satisfactory than for the proton. The most precise experiment which has been performed at TRIUMF by studying the inverse reaction $\pi^- p \rightarrow \gamma n$ [25], is restricted to energies below the Δ resonance. In Fig. 11 it can be seen that we fit this experiment very well. However, to take account of a larger energy range, we had to include older data which are reasonably well described within the larger statistical uncertainties (see Fig. 12).

The parameters determined by our fit have no direct physical interpretation. Given the integral equations, the coefficients of the homogeneous solutions have to be determined by the boundary conditions determined by the physics. Concerning the coupling constants of the vector mesons, we expect them to be of the same order of magnitude as the corresponding values of other analyses. In Tab. II we compare our results with other references. The existing differences should be attributed to the fact part of the vector meson strength is already contained in the dispersive integral up to 2 GeV.

VI. RESULTS, PREDICTIONS AND DISCUSSION

A. S and P wave multipoles

In Figs. 13–16 we show the isospin components of the S - and P -wave multipoles with $I = 0, \frac{1}{2}, \frac{3}{2}$. The solid lines show the results for the real and imaginary parts of the “global fit” obtained with the complete data set. The error bands (dashed lines) result from the errors in the parameters as determined from the covariance matrix after normalizing χ^2 to 1. Because of the relatively small number of parameters, the errors of the global fit are very small except for the components of E_{0+} and M_{1-} with $I = 0$, which reflects the uncertainty of the neutron data. In order to visualize the fluctuations of the data, we also analysed them in bins of 20 MeV with the same parametrization (“local fit”). Except for π^0 production on the proton, the data basis for energies $E_\gamma < 210 \text{ MeV}$ is quite unsatisfactory. As a result we find the largest error bars for all amplitudes in this region. Figs. 17–20 show the decomposition of the isospin $\frac{1}{2}$ amplitudes into proton and neutron part according to Eqs. (19). In this case, the corresponding local fit

was obtained by first fitting the ${}_pM^{(\frac{1}{2})}$ and $M^{(\frac{3}{2})}$ components to the proton data, and then determining the ${}_nM^{(\frac{1}{2})}$ amplitudes by a fit to the neutron data. In the case of the proton, the local fit is in general agreement with the result of the global fit, while we find strong fluctuations and large error bars for the neutron amplitudes. It is obvious that more and better neutron data are needed to get full information on the amplitudes E_{0+} and M_{1-} in the isospin $\frac{1}{2}$ channel, which are of special interest for studies of the associated resonances S_{11} and P_{11} .

Given the results for the S and P waves from our fit, we now turn to a detailed study of the threshold amplitudes for both charged and neutral pions and to the electromagnetic excitation of the $\Delta(1232)$.

B. Low energy amplitudes

As pointed out before, our data basis does not include the threshold region. The main reason for this is that we have to expect isospin symmetry breaking in that region due to the pion mass splitting, while our dispersion calculation is based on the isospin symmetry of the pion-nucleon phase shifts. Therefore, the threshold S wave amplitudes given below are a prediction, in the sense that the cross sections above $E_\gamma = 160$ MeV determine the threshold values by continuation of the analytic functions constructed in dispersion theory [26]. Table III compares our threshold values for the charged pion channels to the “classical” low energy theorem [27] (LET), chiral perturbation theory [28,29] (ChPT) and experiment. Note that ChPT contains lowest order loop corrections, while LET is based on tree graphs only. The agreement between our calculation and the experiment is excellent.

It should be noted that a larger value for $E_{0+}(\pi^-p)$, namely -34.7 ± 1.0 (here and in the following in units of $10^{-3}/m_\pi$), was reported [30]. However, this value derived from angular distributions was recently withdrawn [31]. Incidentally, that (wrong) value would have resulted in a difference of $a_1 - a_3 = 0.275/m_\pi$ for the pion-nucleon scattering lengths, while the (correct) value of Tab. III gives a smaller value of $(0.253 \pm 0.003)/m_\pi$. However, the larger value would be in much better agreement with the analysis of pion-nucleon scattering by the Karlsruhe group [1] and recent results from pionic atoms which lead to a value of $(0.276 \pm 0.013)/m_\pi$ [32]. Since this cross relation between hadronic and electromagnetic physics is only based on the well-known Panofsky ratio, $\sigma(\pi^-p \rightarrow \pi^0n) / \sigma(\pi^-p \rightarrow \gamma n)$, even the small deviation in $a_1 - a_3$ poses a problem. Fig. 21 compares our results to the angular distributions near threshold measured at TRIUMF [31]. With the exception of the data at 165 MeV we find excellent agreement.

Neutral pion photoproduction near threshold has been a topic of many experimental and theoretical investigations in the 90’s. The classical LET predicted a power series expansion of the amplitude in $\mu = m_\pi/m_N \approx 1/7$, leading to a threshold value of about -2.4 plus presumably small corrections in μ^3 . The experimental findings at Saclay [33], Mainz [34] and now at Saskatoon [35] are a considerably different amplitude of about half that value. The classical LET was based on Lorentz, gauge and chiral invariance [27]. It further assumed that the amplitudes are analytical functions, though $\ln \mu$ singularities due to pion loops had been occasionally discussed in the literature. The first consistent calculation of pion photoproduction to one-loop order in ChPT clearly showed the breakdown of analyticity. The result is the expansion [36]

$$E_{0+}(p\pi^0) = \frac{eg_{\pi N}}{8\pi m_\pi} \left(\mu - \mu^2 \frac{3 + \kappa_p}{2} - \mu^2 \frac{m_N^2}{16f_\pi^2} + [\mu^3] \right), \quad (58)$$

with the first two terms on the *rhs* given by the old LET, and the third term a correction due to pion loops. With the numerical values for the anomalous moment κ_p , the nucleon mass m_N , and the pion decay constant $f_\pi = 93$ MeV, this correction even changes the sign of the threshold amplitude. Various predictions are compared with the experiment in Tab. III. The value given by ChPT was recently evaluated in the heavy baryon formalism up to order p^4 [29]. Our value from dispersion theory is obtained by breaking isospin symmetry explicitly by the physical masses of the pions and by assuming that the imaginary parts of the amplitudes start at charged pion threshold and are given by the results of our global fit, i.e. by iteration of Eq. (50) under the stated assumptions. The agreement with experiment is astounding. Once more the data at the higher energies “predict” the threshold values with a good accuracy. This result is particularly surprising, because the real part of E_{0+} obtains very large distributions from the imaginary parts of the higher multipoles via the dispersion integrals. Altogether these contributions nearly cancel the large contribution of the nucleon pole, which corresponds to the result of pseudoscalar coupling, leading to a total threshold value

$$\text{Re}E_{0+}^{\text{thr}}(p\pi^0) = -7.63 + 4.15 - 0.41 + 2.32 + 0.29 + 0.07 = -1.22, \quad (59)$$

$$\text{Re}E_{0+}^{\text{thr}}(n\pi^0) = -5.23 + 4.15 - 0.41 + 3.68 - 0.93 - 0.05 = 1.19, \quad (60)$$

where the individual contributions on the *rhs* are, in that order, the pole term, $M_{1+}, E_{1+}, E_{0+}, M_{1-}$ and higher multipoles. We add that the existing uncertainties for the neutron value of M_{1-} give rise to large effects. Fig. 22 compares our results to the measured angular distributions and predicts values for the three single polarization observables. The dotted curves are obtained by arbitrarily reducing M_{1-} by 50 %, which demonstrates the strong sensitivity of Σ and P with regard to that multipole. Finally, Fig. 23 shows the energy dependence of E_{0+} in the threshold region. The existence of a Wigner cusp in $\text{Re}E_{0+}(p\pi^0)$ at charged pion threshold is due to the infinite derivative of $\text{Im}E_{0+}$ at that threshold, and a reflection of the coupling to the much stronger π^+ channel. We also calculated the threshold values for the three P waves and find agreement with the prediction of ChPT and experimental data within 5-10 %. For a detailed discussion see Ref. [26].

C. The ratio E_{1+}/M_{1+} in the Δ region

The search for a deformation of the “elementary” particles is a longstanding issue. Such a deformation is evidence for a strong tensor force between the constituents, originating in the case of the nucleon from the residual force of gluon exchange between the quarks. Depending on one’s favourite model, such effects can be described by d-state admixture in the quark wave function, tensor correlations between the pion cloud and the quark bag, or by exchange currents accompanying the exchange of mesons between the quarks. Unfortunately, it would require a target with a spin of at least 3/2 (e.g. Δ matter) to observe a static deformation. The only realistic alternative is to measure the transition quadrupole moment between the nucleon and the Δ , i.e. the amplitude E_{1+} . While the existence of such a transition cannot be regarded as direct proof of a deformation, it is sensitive to model parameters responsible for possible deformations of the hadrons.

The experimental quantity of interest is the ratio $R_{EM} = E_{1+}/M_{1+}$ in the region of the Δ . The quark model with SU(6) symmetry predicts $R_{EM} = 0$. Depending on the size of the hyperfine interaction and the bag radius, broken SU(6) leads to $-2\% < R_{EM} < 0$ [37,38]. Similar results can be obtained in the cloudy bag model [39,40], larger effects with Skyrmons [41] ($-5\% < R_{EM} < -2\%$). Exchange currents [42] yield values of about -3.5% . The first lattice QCD results are $(+3 \pm 9)\%$ [43]. The analysis of the data changes by time and method, with a PDG average of $(-1.5 \pm 0.4)\%$ [44].

The comparison of our dispersion analysis [45] with the analysis of the Mainz data by Beck et al. [46] shows nice agreement with the multipole M_{1+} but systematic differences for the quadrupole transition E_{1+} at energies above the resonance. However, the ratio R_{EM} at resonance agrees quite well in both analyses (see Fig. 24). Unfortunately, there appears to be a discrepancy of up to 15 % between the differential cross sections measured at Mainz (upon which our analysis is largely based) and the LEGS data [47] at Brookhaven. As far as ratios of cross sections are concerned, the data seem to be in general agreement. As an example, the ratio of the LEGS cross sections for photons with polarization parallel and orthogonal to the scattering plane [48], is nicely described by our analysis (see Fig. 25), though these data have not been included in our fit. In view of the importance of the quantity R_{EM} for our understanding of the internal structure of the nucleon, the existing discrepancies between the data deserve further studies. Based on “our” data selection we obtain a value $R_{EM} = (-2.5 \pm 0.1)\%$ for the global fit ($(-2.33 \pm 0.17)\%$ for the local fit), which is close to the value derived by Beck et al. [49].

Another point of interest is the separation of resonance and background contributions. The problem in this quest arises, because the leading tree graphs, the Born terms and the Δ excitation, do not fulfill the requirements of unitarity (Fermi-Watson theorem). In physical terms, the pion produced by the Born graph feels the presence of the resonance and is reabsorbed by the nucleon to form a Δ , which altogether leads to the required phase relation of Eq. (28). Together with the “pure” Δ , these diagrams constitute the “dressed” Δ . A technique to achieve this result is the method of Olsson [50],

$$M_{1+} = |M_{1+}^B|e^{i\delta_B} + |M_{1+}^{\text{res}}|e^{i\delta_{\text{res}}}e^{i\Phi} = |M_{1+}|e^{i\delta_{1+}}, \quad (61)$$

which combines the two contributions, unitarized individually, by a rotation of the resonance contribution in the complex plane. The other technique is the K-matrix method [51],

$$K(W) = A(W)/(M_{\text{res}} - W) + B(W), \quad (62)$$

$$T(W) = K(W)\cos\delta(W)e^{i\delta(W)}, \quad (63)$$

where $B(W)$ is a slowly varying background, and $\delta(W = M_{\text{res}}) = \pi/2$. It is obvious that different approaches will give different answers to the question which part of ratio R_{EM} is due to the “pure” resonance.

Due to the analyticity of the functions involved, dispersion theory is particularly apt to study the amplitudes in the complex energy plane. Therefore, we have analyzed the amplitude by comparing the “speed” [52]

$$SP[M_{1+}(W)] = \left| \frac{dM_{1+}(W)}{dW} \right| \quad (64)$$

with the speed of an ideal resonance due to a pole in the complex plane at $W_R = M_R - i\Gamma_R/2$. Such a resonance has the amplitude

$$M_{1+}^{\text{res}}(W) = \frac{re^{i\Phi}\Gamma_R}{M_R - W - i\Gamma_R/2} \quad , \quad (65)$$

with $re^{i\Phi}$ determining the complex residue at resonance, $W = W_R$.

Due to the differentiation involved, the effect of a slowly varying background is much reduced, and the “experimental” speed agrees nicely with the “ideal” speed, as can be seen in Fig. 26 (left part). The same is true for the speed vector, the complex number dM_{1+}/dW , which has been plotted on the *rhs* of Fig. 26. The experimental values given by the crosses in this figure agree quite well with the squares of the ideal resonance, except for the smallest energies close to the origin. We note that as function of energy W the values run counter-clockwise, starting near the origin at threshold (the “stem” of the apple-shaped structure), passing through resonance at maximum speed (the “blossom” of the apple), and again approaching the origin for $W \rightarrow \infty$. The fact that the “apples” for M_{1+} (top) and E_{1+} (bottom) are essentially oriented in opposite directions is related to the negative value of R_{EM} . The phases of the complex amplitudes at resonance are defined by the angles Φ_M and Φ_E respectively (see Fig. 26). Table IV shows our results for the pole position and the complex residue at the pole for both the magnetic dipole and the electric quadrupole transitions. The complex ratio of the residues is given by

$$R_{EM}^{\Delta} = \frac{re^{i\Phi}(E_{1+})}{re^{i\Phi}(M_{1+})} = -0.035 - 0.046i. \quad (66)$$

The values for the pole position are in perfect agreement with the analysis of pion-nucleon scattering. Essentially based on analyses of Höhler et al., the PDG [44] lists $M_R = (1210 \pm 1)$ MeV and $\Gamma_R = (100 \pm 2)$ MeV. The complex ratio R_{EM}^{Δ} at the Δ pole, $W = M_R - i\Gamma_R/2$, is rather stable in comparison with the value R_{EM} on the real axis, at $W = M_{\text{res}} \approx 1232$ MeV. As an example, Sato et al. [53] have studied two versions of a dynamical model leading to a difference in R_{EM}^{Δ} of 30 % while R_{EM} differs by as much as 300 %! It is also worth noting that studies of hyperon resonance radiative decay in the framework of ChPT have predicted values for R_{EM}^{Δ} compatible with our results within the error bars. Finally, Fig. 27 shows the resonance-background separation of the real and imaginary parts for the two Δ multipoles. Indeed, the speed-plot technique leads to a slowly varying background except for the threshold region where the background has to cancel the “ideal” resonance shape to give the (vanishing) physical amplitude. While the experimental amplitude E_{1+} , particularly its real part, is quite different from a typical resonance shape, the amplitude after background subtraction is not too far from an ideal resonance. It is in fact rather astounding that M_R can be predicted to four digits and Γ_R to two digits from the E_{1+} amplitude, which is about half resonance and half background (see Fig. 27).

Instead of the multipoles the electromagnetic resonance excitation is very often discussed in terms of helicity amplitudes. In Tab. V we give the helicity matrix elements $A_{\frac{1}{2}}$ and $A_{\frac{3}{2}}$ for the transition $\gamma N \rightarrow \Delta$ which are derived from our results for the multipoles via the standard definitions. In that table also the ratio R_{EM} is given which is equivalent to the result of the application of the K-matrix method.

D. Total cross sections

As a result of our fit we also obtain predictions for the total cross sections. These are shown in Fig. 28 for the four physical reactions, together with the contributions of the leading S - and P -wave multipoles. In terms of the multipoles, the total cross sections are

$$\sigma_{\text{tot}} = 2\pi \frac{|\vec{k}|}{|\vec{q}|} \sum_{l=0}^{\infty} (l+1)^2 \left[(l+2) (|E_{l+}|^2 + |M_{l+1,-}|^2) + l (|M_{l+}|^2 + |E_{l+1,-}|^2) \right]. \quad (67)$$

with the isospin combinations of the multipoles according to Eqs. (14–17).

A topic of much current interest is the spin structure of the total absorption cross section, which will be measured with circularly polarized photons and nucleon target polarization in the direction of the photon momentum [54,55]. Depending on their relative direction, the spins of photon and nucleon add to spin 3/2 or subtract to spin 1/2, which defines the helicity structure of the total cross sections, $\sigma_{\frac{3}{2}}$ and $\sigma_{\frac{1}{2}}$, with $\sigma_{tot} = (\sigma_{\frac{3}{2}} + \sigma_{\frac{1}{2}})/2$. The difference of these two quantities enters into the Gerasimov-Drell-Hearn (GDH) sum rule,

$$-\frac{\kappa^2}{4} = \frac{m_N^2}{8\pi^2\alpha} \int_{\nu_{thr}}^{\infty} \frac{d\nu}{\nu} \left(\sigma_{\frac{1}{2}}(\nu) - \sigma_{\frac{3}{2}}(\nu) \right), \quad (68)$$

which relates the helicity structure of the total absorption cross section of the nucleon with its ground state properties. Our prediction for the contributions of single pion production to $\sigma_{\frac{3}{2}} - \sigma_{\frac{1}{2}}$ and the GDH integral as function of its upper limit E_γ is shown in Fig. 29.

VII. SUMMARY AND OUTLOOK

Dispersion relations at fixed t provide a useful framework to analyze pion photoproduction between threshold and an excitation energy of about 500 MeV. After multipole projection we obtain a system of coupled integral equations for the multipole amplitudes whose solutions depend on 10 free parameters, which are fitted to selected experimental data in the range of $160 \text{ MeV} \leq E_\gamma \leq 420 \text{ MeV}$. On the basis of these amplitudes, we obtain predictions for the threshold behaviour of pion photoproduction, including the cusp effect for neutral pion production. The results for S and P waves agree within about 5 - 10 % with the predictions of ChPT and a direct analysis of the threshold data.

In the region of the $\Delta(1232)$, we find a ratio of the electric quadrupole to the magnetic dipole amplitude of $R_{EM} = (-2.5 \pm 0.1)\%$ at $W = M_{res} = 1232 \text{ MeV}$. The Δ resonance pole in the complex plane can be determined from both amplitudes, in excellent agreement with the results of pion-nucleon scattering. The ratio of the complex residues at the pole is $R_{EM}^\Delta = (-3.5 - 4.6i)\%$. While R_{EM} is very model dependent, the value at the resonance pole is relatively stable.

Since our “global fit” contains only relatively few parameters, it cannot follow all the fluctuations of the data in the energy and angular distributions. Therefore, the overall χ^2 is only 2.8 per data point. We are convinced that many of the fluctuations of the data are due to systematical errors and, therefore, should not be reproduced by a theoretical analysis. In order to obtain an estimate of such systematical errors, we also show the result of a “local fit” by fitting the free parameters to, e.g., the data in 20 MeV bins individually.

As further tests of the remaining model dependence of our procedure, we are presently studying some modifications of the parametrization. First, the high t -channel contributions to the dispersion integrals will be replaced by a Regge model. Second, all isospin components of the S , P and D waves will be treated on the same footing by allowing for the addition of homogeneous solutions to all of them. The explicit fit of all D wave contributions will give the possibility to study the influence of the higher partial waves.

In conclusion we have obtained a good representation of the data in the range up to about 500 MeV. The biggest experimental uncertainties are shown to be due to the neutron data, in particular in the case of the E_{0+} and M_{1-} amplitudes. New experiments to determine the small amplitudes by polarization observables are urgently needed, particularly in the case of the neutron and the Roper multipoles.

APPENDIX A: MATRICES CONNECTING THE AMPLITUDES

The matrices connecting the various amplitudes defined in the text are:

$$\mathbf{H} = \text{diag} \left(\begin{array}{c} \frac{\sqrt{(E_f+m_N)(E_i+m_N)}(W-m_N)}{8\pi W} \\ \frac{\sqrt{(E_i+m_N)}(W-m_N)|\vec{k}|}{\sqrt{E_f+m_N} 8\pi W} \\ \frac{\sqrt{(E_f+m_N)(E_i+m_N)}(W-m_N)|\vec{k}|}{8\pi W} \\ \frac{\sqrt{E_i+m_N}(W-m_N)|\vec{k}|^2}{\sqrt{E_f+m_N} 8\pi W} \end{array} \right), \quad (A1)$$

$$\mathbf{C} = \begin{pmatrix} 1 & 0 & -\frac{t-m_\pi^2}{2(W-m_N)} & W-m_N + \frac{t-m_\pi^2}{2(W-m_N)} \\ -1 & 0 & -\frac{t-m_\pi^2}{2(W+m_N)} & W+m_N + \frac{t-m_\pi^2}{2(W+m_N)} \\ 0 & W-m_N & 1 & -1 \\ 0 & -(W+m_N) & 1 & -1 \end{pmatrix}, \quad (\text{A2})$$

$$\mathbf{C}^{-1} = \frac{1}{4W^2} \begin{pmatrix} (C^{-1})_{11} & (C^{-1})_{12} & (C^{-1})_{13} & (C^{-1})_{14} \\ 0 & 0 & 2W & -2W \\ 2W & 2W & (C^{-1})_{33} & (C^{-1})_{34} \\ 2W & 2W & W\frac{t-m_\pi^2}{W-m_N} & W\frac{t-m_\pi^2}{W+m_N} \end{pmatrix}, \quad (\text{A3})$$

with

$$\begin{aligned} (C^{-1})_{11} &= 2W(W+m_N), \\ (C^{-1})_{12} &= -2W(W-m_N), \\ (C^{-1})_{13} &= 2m_N W \frac{t-m_\pi^2}{W-m_N}, \\ (C^{-1})_{14} &= 2m_N W \frac{t-m_\pi^2}{W+m_N}, \\ (C^{-1})_{33} &= 2W \left(W+m_N + \frac{t-m_\pi^2}{2(W-m_N)} \right), \\ (C^{-1})_{34} &= 2W \left(W-m_N + \frac{t-m_\pi^2}{2(W+m_N)} \right). \end{aligned}$$

$$\mathbf{G}_l(x) = \begin{pmatrix} P'_{l+1}(x) & P'_{l-1}(x) & lP'_{l+1}(x) & (l+1)P'_{l-1}(x) \\ 0 & 0 & (l+1)P'_l(x) & lP'_l(x) \\ P''_{l+1}(x) & P''_{l-1}(x) & -P''_{l+1}(x) & P''_{l-1}(x) \\ -P''_l(x) & -P''_l(x) & P''_l(x) & -P''_l(x) \end{pmatrix}, \quad (\text{A4})$$

$$\mathbf{D}_l(x) = \begin{pmatrix} \frac{1}{2(l+1)}\{P_l & -P_{l+1} & \frac{l}{2l+1}(P_{l-1}-P_{l+1}) & \frac{l+1}{2l+3}(P_l-P_{l+2})\} \\ \frac{1}{2l}\{P_l & -P_{l-1} & \frac{l+1}{2l+1}(P_{l+1}-P_{l-1}) & \frac{l}{2l-1}(P_l-P_{l-2})\} \\ \frac{1}{2(l+1)}\{P_l & -P_{l+1} & \frac{1}{2l+1}(P_{l+1}-P_{l-1}) & 0\} \\ \frac{1}{2l}\{-P_l & P_{l-1} & \frac{1}{2l+1}(P_{l-1}-P_{l+1}) & 0\} \end{pmatrix}, \quad (\text{A5})$$

with the Legendre polynomials P_l as functions of x .

The entries of the matrix \mathbf{E} are:

$$\begin{aligned} E_{11}^I &= \frac{1}{W'-W} + \frac{\varepsilon^I}{W'^2-u} \left(W'+W + \frac{t-m_\pi^2}{W-m_N} \right), \\ E_{12}^I &= -\frac{1}{W'+W} + \frac{\varepsilon^I}{W'^2-u} \left(W-W' + \frac{t-m_\pi^2}{W-m_N} \right), \\ E_{13}^I &= -\frac{1-\varepsilon^I}{2} \frac{t-m_\pi^2}{(W'-m_N)(W-m_N)}, \\ E_{14}^I &= -\frac{1-\varepsilon^I}{2} \frac{t-m_\pi^2}{(W'+m_N)(W-m_N)}, \\ E_{21}^I &= -\frac{1}{W'+W} + \frac{\varepsilon^I}{W'^2-u} \left(W-W' + \frac{t-m_\pi^2}{W+m_N} \right), \\ E_{22}^I &= \frac{1}{W'-W} - \frac{\varepsilon^I}{W'^2-u} \left(W'+W + \frac{t-m_\pi^2}{W+m_N} \right), \\ E_{23}^I &= -\frac{1-\varepsilon^I}{2} \frac{t-m_\pi^2}{(W'-m_N)(W+m_N)}, \end{aligned}$$

$$\begin{aligned}
E_{24}^I &= -\frac{1-\varepsilon^I}{2} \frac{t-m_\pi^2}{(W'+m_N)(W+m_N)}, \\
E_{31}^I &= -\frac{2\varepsilon^I}{W'^2-u}, \\
E_{32}^I &= -\frac{2\varepsilon^I}{W'^2-u}, \\
E_{33}^I &= \frac{1}{W'-W} + \frac{\varepsilon^I}{W'^2-u} \left(W-W'-2m_N - \frac{t-m_\pi^2}{W-m_N} \right), \\
E_{34}^I &= \frac{1}{W'+W} + \frac{\varepsilon^I}{W'^2-u} \left(-W'-W+2m_N - \frac{t-m_\pi^2}{W+m_N} \right), \\
E_{41}^I &= -\frac{2\varepsilon^I}{W'^2-u}, \\
E_{42}^I &= -\frac{2\varepsilon^I}{W'^2-u}, \\
E_{43}^I &= \frac{1}{W'+W} + \frac{\varepsilon^I}{W'^2-u} \left(-W'-W-2m_N - \frac{t-m_\pi^2}{W'-m_N} \right), \\
E_{44}^I &= \frac{1}{W'-W} + \frac{\varepsilon^I}{W'^2-u} \left(W-W'+2m_N - \frac{t-m_\pi^2}{W'+m_N} \right).
\end{aligned} \tag{A6}$$

APPENDIX B: RESPONSE FUNCTIONS

The response functions discussed in this contribution may be expressed by the CGLN amplitudes as follows:

$$\begin{aligned}
R_T &= |\mathcal{F}_1|^2 + |\mathcal{F}_2|^2 + \frac{1}{2} \sin^2 \theta (|\mathcal{F}_3|^2 + |\mathcal{F}_4|^2) \\
&\quad - \text{Re}\{2 \cos \theta \mathcal{F}_1^* \mathcal{F}_2 - \sin^2 \theta (\mathcal{F}_1^* \mathcal{F}_4 + \mathcal{F}_2^* \mathcal{F}_3 + \cos \theta \mathcal{F}_3^* \mathcal{F}_4)\}, \\
R_T^{n_i} &= \sin \theta \text{Im}\{\mathcal{F}_1^* \mathcal{F}_3 - \mathcal{F}_2^* \mathcal{F}_4 + \cos \theta (\mathcal{F}_1^* \mathcal{F}_4 - \mathcal{F}_2^* \mathcal{F}_3) - \sin^2 \theta \mathcal{F}_3^* \mathcal{F}_4\}, \\
R_T^{n_f} &= -\sin \theta \text{Im}\{2\mathcal{F}_1^* \mathcal{F}_2 + \mathcal{F}_1^* \mathcal{F}_3 - \mathcal{F}_2^* \mathcal{F}_4 + \cos \theta (\mathcal{F}_1^* \mathcal{F}_4 - \mathcal{F}_2^* \mathcal{F}_3) - \sin^2 \theta \mathcal{F}_3^* \mathcal{F}_4\}, \\
R_{TT} &= \sin^2 \theta \left(\frac{1}{2} (|\mathcal{F}_3|^2 + |\mathcal{F}_4|^2) + \text{Re}\{\mathcal{F}_1^* \mathcal{F}_4 + \mathcal{F}_2^* \mathcal{F}_3 + \cos \theta \mathcal{F}_3^* \mathcal{F}_4\} \right).
\end{aligned}$$

APPENDIX: ACKNOWLEDGMENTS

We would like to thank Prof. G. Höhler for very fruitful discussions and the members of the A2 collaboration at Mainz for providing us with their preliminary data, in particular J. Arends, R. Beck, F. Härter, H.-P. Krahn and H. Ströher as well as G. Anton from ELSA at Bonn. This work was supported by the Deutsche Forschungsgemeinschaft (SFB 201).

-
- [1] G. Höhler, Pion–Nucleon Scattering, Landoldt-Börnstein, Vol.I/9b2, ed. H. Schopper, Springer (1983).
 - [2] I. S. Barker, A. Donnachie and J. K. Storrow, Nucl. Phys. B 95 (1975) 347.
 - [3] D. Schwela and R. Weizel, Z. Physik 221 (1969) 71.

- [4] G. F. Chew et al., Phys. Rev. 106 (1957) 1345.
- [5] J. D. Bjorken and S. D. Drell, Relativistic Quantum Mechanics, McGraw-Hill, New York (1964).
- [6] K. M. Watson, Phys. Rev. 182 (1954) 228.
- [7] D. Drechsel and L. Tiator, J. Phys. G 18 (1992) 449.
- [8] J. S. Ball, Phys. Rev. 124 (1961) 2014.
- [9] F. A. Berends, A. Donnachie and D. L. Weaver, Nucl. Phys. B 4 (1967) 1.
- [10] O. Hanstein, Ph.D. thesis, Mainz (1996).
- [11] R. Omnès, Nuovo Cim. 8 (1958) 316.
- [12] A. I. Lebedev und B. V. Mangazeyev in A. A. Komar (ed.), Photoproduction of Pions on Nucleons and Nuclei, Nova Science Publishers, New York and Budapest (1989).
- [13] A. Donnachie in E. U. S. Burhop (ed.), High Energy Physics, Vol. V, Academic Press, New York (1972).
- [14] R. A. Arndt, I. I. Strakovsky and R. L. Workman, Phys. Rev. C 52 (1995) 2120.
- [15] M. Fuchs et al., Phys. Lett. B 368 (1996) 20,
M. Fuchs, Ph.D. thesis, Gießen (1996).
- [16] H.-P. Krahn, Ph.D. thesis, Mainz (1996),
R. Beck, H.-P. Krahn et al., Phys. Rev. Lett. 78 (1997) 606.
- [17] F. Haerter, Ph.D. thesis, Mainz (1996).
- [18] D. Menze, W. Pfeil und R. Wilcke, Compilation of Pion Photoproduction Data, Bonn (1977).
- [19] K. Büchler et al., Nucl. Phys. A 570 (1994) 580.
- [20] H. Dutz, Ph.D. thesis, Bonn (1993),
D. Krämer, Ph.D. thesis, Bonn (1993),
B. Zucht, Ph.D. thesis, Bonn (1995),
H. Dutz et al., Nucl. Phys. A 601 (1996) 319..
- [21] M. Beneventano et al., Nuovo Cim. 4 (1958) 323.
- [22] F. Carbonara et al., Nuovo Cim. 13 A (1973) 59.
- [23] P. Benz et al., Nucl. Phys. B 65 (1973) 158.
- [24] T. Fuji et al., Nucl. Phys. B 120 (1977) 395.
- [25] A. Bagheri et al., Phys. Rev. C 38 (1988) 875.
- [26] O. Hanstein, D. Drechsel and L. Tiator, Phys. Lett. B 399 (1997) 13.
- [27] P. de Baenst, Nucl. Phys. B 24 (1970) 633.
- [28] V. Bernard, N. Kaiser and U.-G. Meißner, Phys. Lett. B 378 (1996) 337.
- [29] V. Bernard, N. Kaiser and U.-G. Meißner, Phys. Lett. B 383 (1996) 116.
- [30] K. Liu, Ph.D. thesis, University of Kentucky (1994).
- [31] M. A. Kovash et al., πN Newsletter 12 (1997) 51.
- [32] D. Sigg et al., Phys. Rev. Lett. 75 (1995) 3245,
D. Sigg et al., Nucl. Phys. A 609 (1996) 269,
M. Janousch et al., Proc. of the 14th Int. Conf. on Particles and Nuclei, Williamsburg 1996, eds. C.E. Carlson, J.J. Domingo, World Scientific, Singapore 1997, p. 372.
- [33] E. Mazzucato et al., Phys. Rev. Lett. 57 (1986) 3144.
- [34] R. Beck et al., Phys. Rev. Lett. 65 (1990) 1841.
- [35] J. C. Bergstrom, Phys. Rev. C 52 (1995) 1986,
J. C. Bergstrom et al., Phys. Rev. C 53 (1996) 1052,
J. C. Bergstrom, R. Igarashi, and J. M. Vogt, Phys. Rev. C 55 (1997) 2016.
- [36] V. Bernard, J. Gasser and U.-G. Meißner, Phys. Lett B 268 (1991) 291.
- [37] R. Koniuk and N. Isgur, Phys. Rev. D 21 (1980) 1868.
- [38] D. Drechsel and M. M. Giannini, Phys. Lett. 143 B (1984) 329.
- [39] G. Kälbermann and J. J. Eisenberg, Phys. Rev. D 28 (1983) 71, and
Phys. Rev. D 29 (1984) 517.
- [40] K. Bermuth, D. Drechsel, L. Tiator and J. B. Seaborn, Phys. Rev. D 37 (1988) 89.
- [41] A. Wirzba and W. Weise, Phys. Lett. B 188 (1987) 6.
- [42] A. Buchmann, E. Hernández and A. Faessler, Phys. Rev. C 55 (1997) 448.
- [43] D. B. Leinweber, et al., Proc. Int. Conf. "Baryons '92", p. 29 (1992).
- [44] Review of Particle Physics, Phys. Rev. D 54 Part I (1996).
- [45] O. Hanstein, D. Drechsel and L. Tiator, Phys. Lett. B 385 (1996) 45.
- [46] R. Beck, Proc. Int. Conf. "Baryons '95", Santa Fé, (1995).
- [47] G. Blanpied et al., preprint BNL-64382, Brookhaven 1997.
- [48] G. Blanpied et al., Phys. Rev. Lett. 69 (1992) 1880,
A. Sandorfi, private communication (1996), release L7a8.0.
- [49] R. Beck et al., Phys. Rev. Lett. 78 (1997) 606.
- [50] M. G. Olsson, Nucl. Phys. B 78 (1974) 55.

- [51] R. M. Davidson and N. C. Mukhopadhyay, Phys. Rev. D 42 (1990) 20.
[52] G. Höhler and A. Schulte, πN Newsletter 7 (1992) 94.
For a detailed discussion and interpretation of the speed of a resonant amplitude see: A. Bohm, Quantum Mechanics: Foundations and Applications, Springer (1993).
[53] T. Sato and T.-S. H. Lee, Phys. Rev. C 54 (1996) 2660.
[54] MAMI proposal A2/2-93, Experimental check of the GDH sum rule, Mainz (1993).
[55] ELSA proposal to measure the GDH sum rule, Bonn (1993).
[56] A. Donnachie, Rep. Prog. Phys. 36 (1973) 695.
[57] R. Machleidt et al., Phys. Rep. 149 (1987) 1.
[58] P. Mergell, diploma thesis, Mainz (1995),
P. Mergell, U.-G. Meißner and D. Drechsel, Nucl. Phys. A 596 (1996) 367.
[59] M. I. Adamovich, Proc. P. N. Lebedev Phys. Inst. 71 (1976) 119.
[60] G. Fischer et al., Z. Phys. 253 (1972) 38.
[61] H. Genzel et al., Z. Phys. 268 (1974) 43.
[62] A. M. Bernstein et al., Phys. Rev. C 55 (1997) 1509.
[63] V. Bernard, N. Kaiser and U.-G. Meißner, Z. Phys. C 70 (1996) 483.
[64] A2 Collaboration at MAMI, private communication (1995).
[65] T. Fuji et al., Phys. Rev. Lett. 28 (1972) 1672.
[66] G. Chiefari et al., Lett. Nuovo Cim. 13 (1975) 129.

TABLE I. Compilation of the data included in our fit. The total number of data points is 1751.

| reaction | observable | E_γ [MeV] | number of data points | reference |
|--------------------------------|-------------------|------------------|-----------------------|-----------|
| $\gamma p \rightarrow \pi^+ n$ | $d\sigma/d\Omega$ | 162–220 | 152 | [18] |
| | $d\sigma/d\Omega$ | 270–420 | 176 | [16] |
| | $d\sigma/d\Omega$ | 247–452 | 61 | [19] |
| | Σ | 270–420 | 176 | [16] |
| | Σ | 211–267 | 36 | [18] |
| | T | 220–425 | 107 | [20] |
| $\gamma p \rightarrow \pi^0 p$ | $d\sigma/d\Omega$ | 160–180 | 224 | [15] |
| | $d\sigma/d\Omega$ | 270–420 | 107 | [16] |
| | $d\sigma/d\Omega$ | 210–425 | 82 | [17] |
| | Σ | 270–420 | 107 | [16] |
| | T | 272–398 | 28 | [20] |
| | | | | |
| $\gamma n \rightarrow \pi^- p$ | $d\sigma/d\Omega$ | 190–420 | 189 | [22] |
| | $d\sigma/d\Omega$ | 190–230 | 20 | [21] |
| | $d\sigma/d\Omega$ | 230–420 | 78 | [23] |
| | $d\sigma/d\Omega$ | 250–420 | 158 | [24] |
| | $d\sigma/d\Omega$ | 194–270 | 50 | [25] |
| | | | | |

TABLE II. Vector meson coupling constants from our fit compared to the values used for the Bonn potential [57] and a dispersion theoretical analysis of nucleon form factors [58].

| | g_ρ^V | g_ρ^T | g_ω^V | g_ω^T |
|-----------|------------|------------|--------------|--------------|
| this work | 4.85 | 15.69 | 6.78 | -1.67 |
| Ref. [57] | 3.24 | 19.81 | 15.85 | 0 |
| Ref. [58] | 1.99 | 12.42 | 20.86 | -3.41 |

TABLE III. The S wave amplitude E_{0+} at threshold in units of $10^{-3}/m_\pi$.

| | $\gamma p \rightarrow \pi^+ n$ | $\gamma n \rightarrow \pi^- p$ | $\gamma p \rightarrow \pi^0 p$ | $\gamma n \rightarrow \pi^0 n$ |
|--------------|--------------------------------|--------------------------------|--------------------------------|--------------------------------|
| “LET” [27] | 27.5 | -32.0 | -2.4 | 0.4 |
| ChPT [28,29] | $28.2 \pm .6$ | $-32.7 \pm .6$ | -1.16 | 2.13 |
| this work | $28.4 \pm .2$ | $-31.9 \pm .2$ | $-1.22 \pm .16$ | $1.19 \pm .16$ |
| experiment | $28.3 \pm .2$ [59] | $-31.8 \pm .2$ [59] | $-1.31 \pm .08$ [15,35] | |

TABLE IV. Result of the speed plot

| | M_R (MeV) | Γ_R (MeV) | $r(10^{-3}/m_\pi)$ | Φ (deg) |
|----------|--------------|------------------|--------------------|--------------|
| M_{1+} | 1212 ± 1 | 99 ± 2 | 21.16 | -27.5 |
| E_{1+} | 1211 ± 1 | 102 ± 2 | 1.23 | -154.7 |

TABLE V. The ratio R_{EM} and the helicity amplitudes $A_{\frac{1}{2}}$ and $A_{\frac{3}{2}}$ for the $\gamma N \rightarrow \Delta$ transition. In determining $A_{\frac{1}{2}}$ and $A_{\frac{3}{2}}$, for the $\Delta(1232)$ a total width of 113 MeV has been assumed.

| | R_{EM} (%) | $A_{\frac{1}{2}} (10^{-3}/\sqrt{\text{GeV}})$ | $A_{\frac{3}{2}} (10^{-3}/\sqrt{\text{GeV}})$ |
|------------|------------------|---|---|
| global fit | -2.54 ± 0.10 | -131.2 | -252.2 |
| local fit | -2.33 ± 0.17 | -129.4 ± 1.3 | -246.6 ± 1.3 |

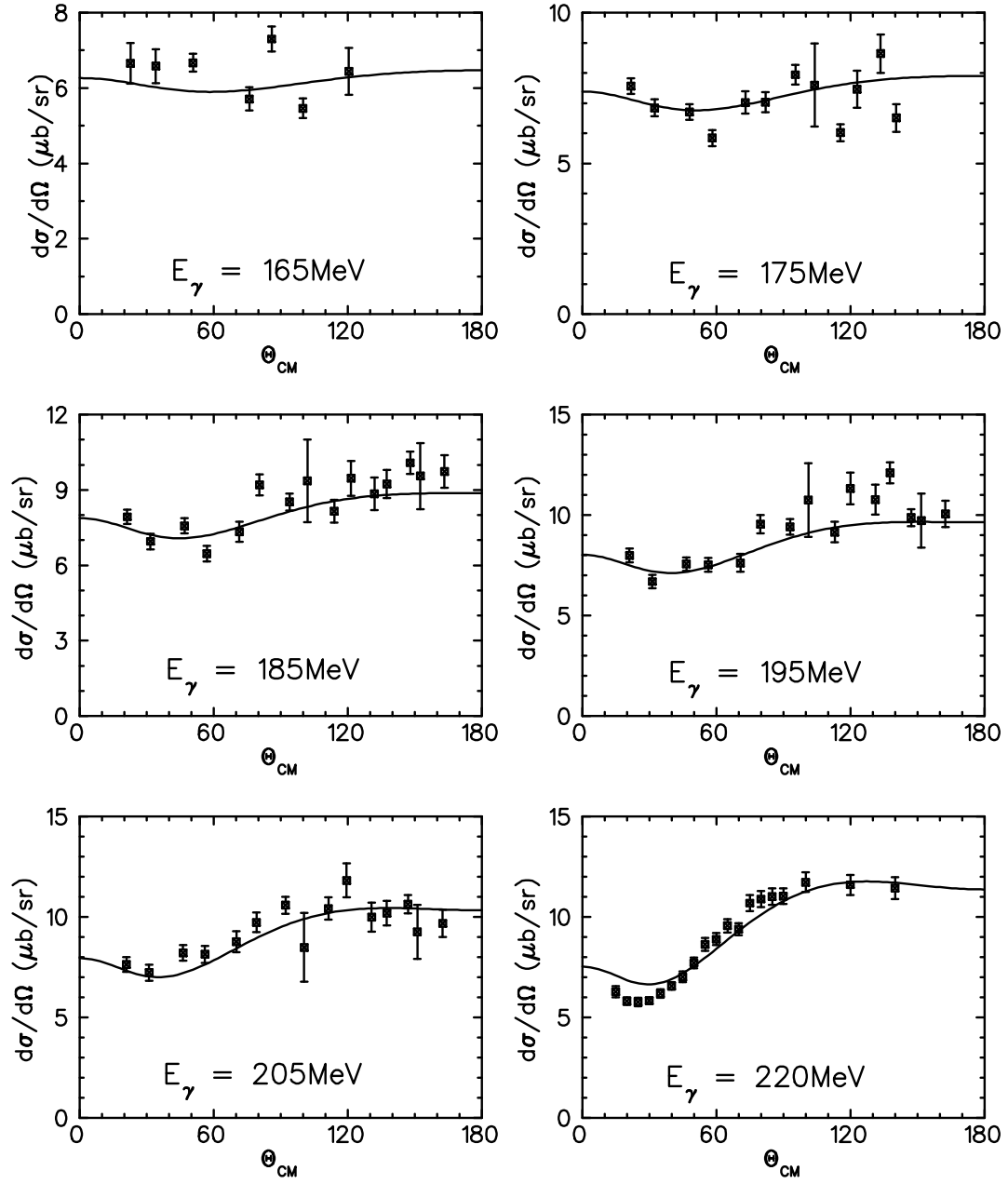


FIG. 1. Differential cross sections for $\gamma p \rightarrow \pi^+ n$ at lower energies. The data are taken from Ref. [18].

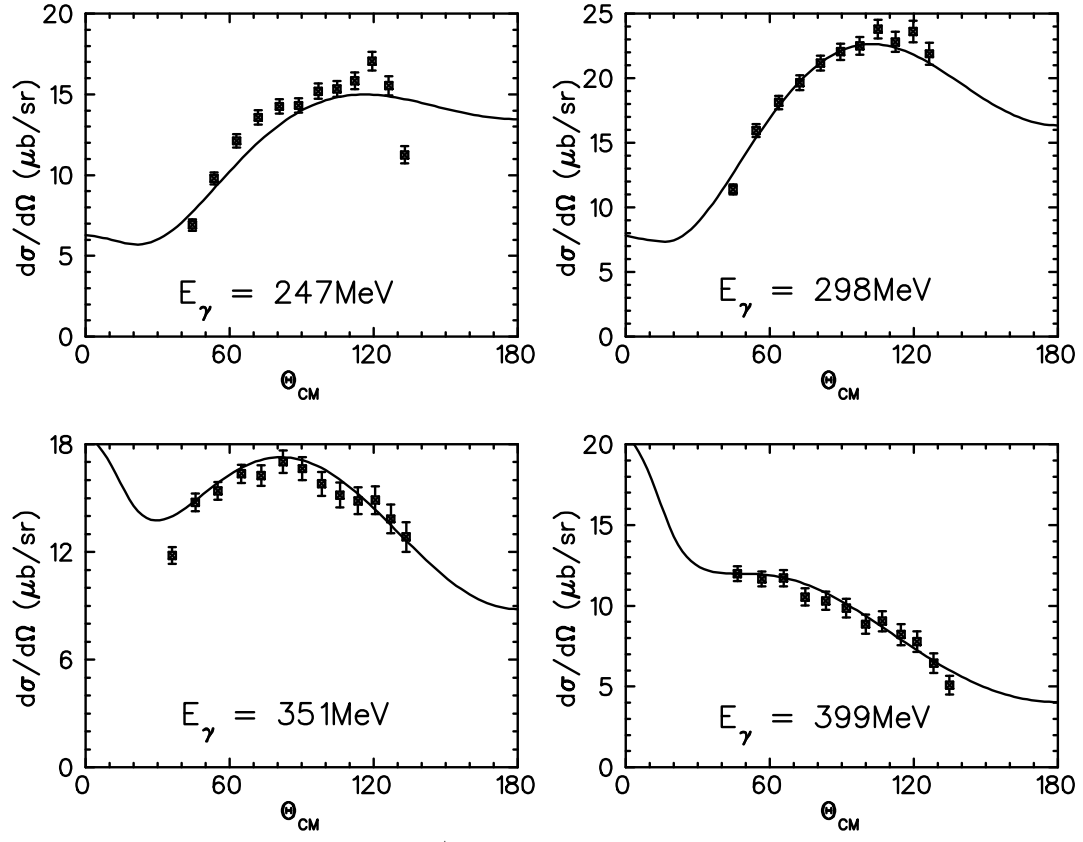


FIG. 2. Differential cross sections for $\gamma p \rightarrow \pi^+ n$ around the $\Delta(1232)$ -resonance. The data are from Bonn [19].

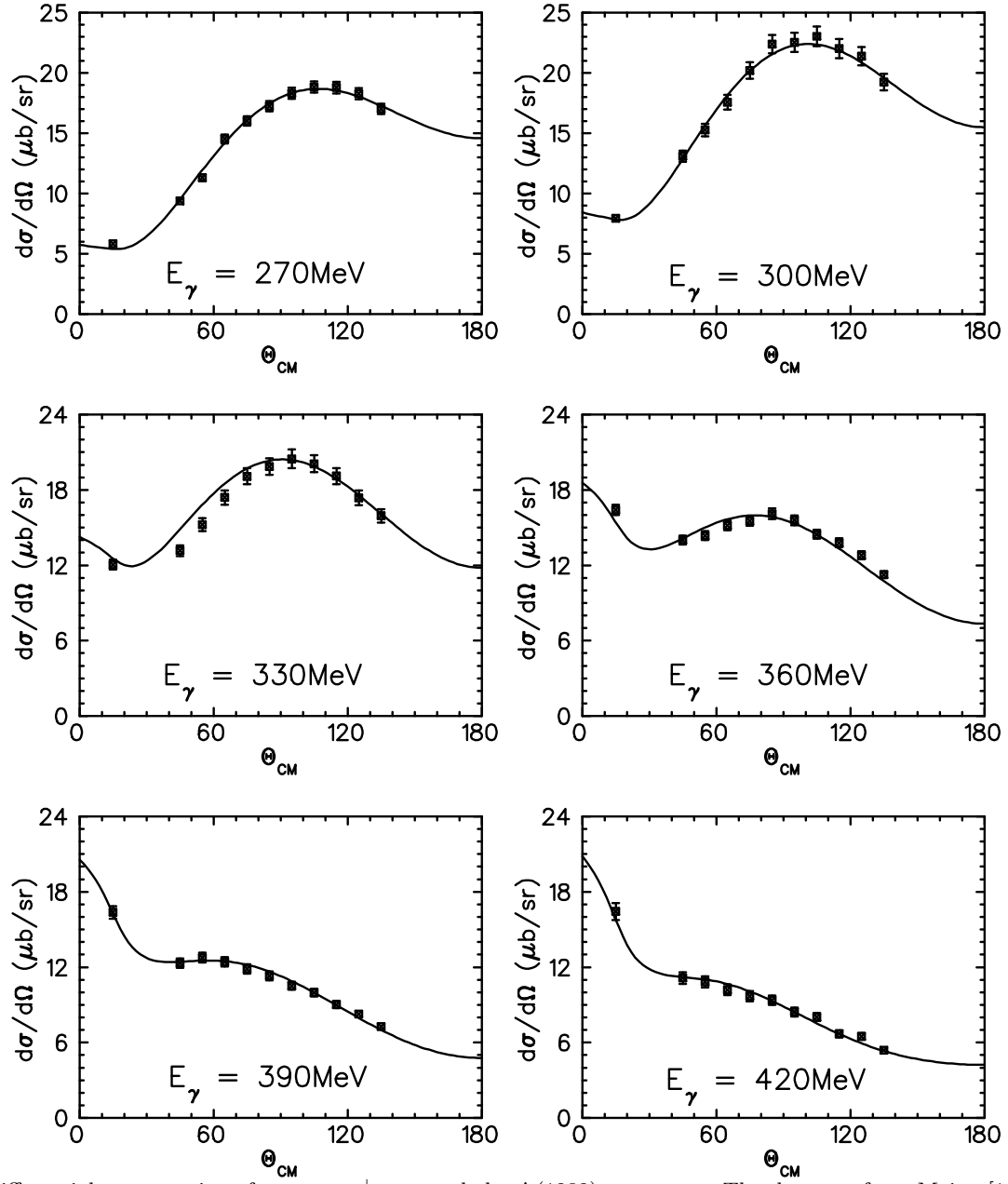


FIG. 3. Differential cross sections for $\gamma p \rightarrow \pi^+ n$ around the $\Delta(1232)$ -resonance. The data are from Mainz [16] except the data for $\theta = 15^\circ$ which are from Bonn [60].

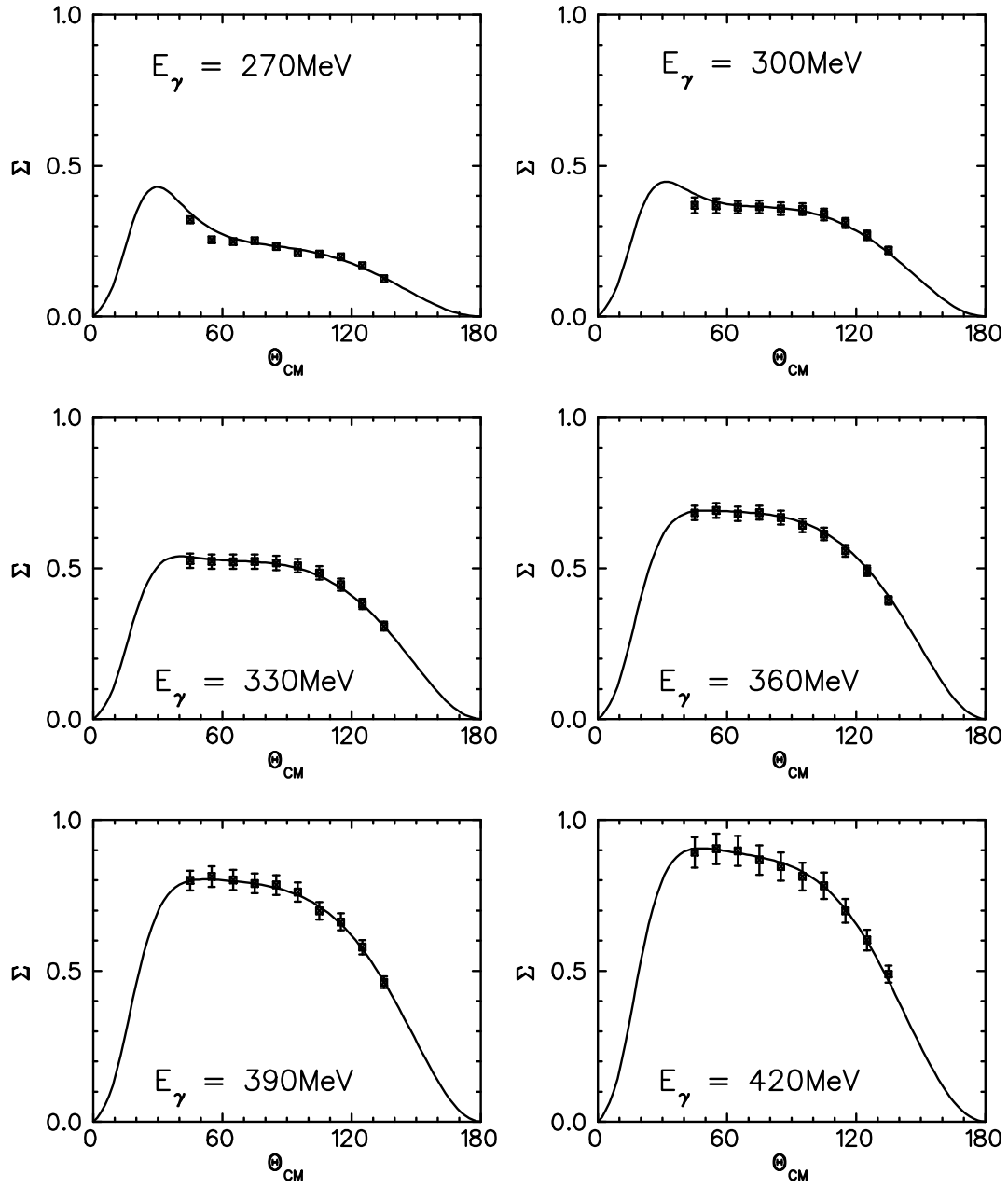


FIG. 4. The beam asymmetry Σ for $\gamma p \rightarrow \pi^+ n$. The data are from Mainz [16].

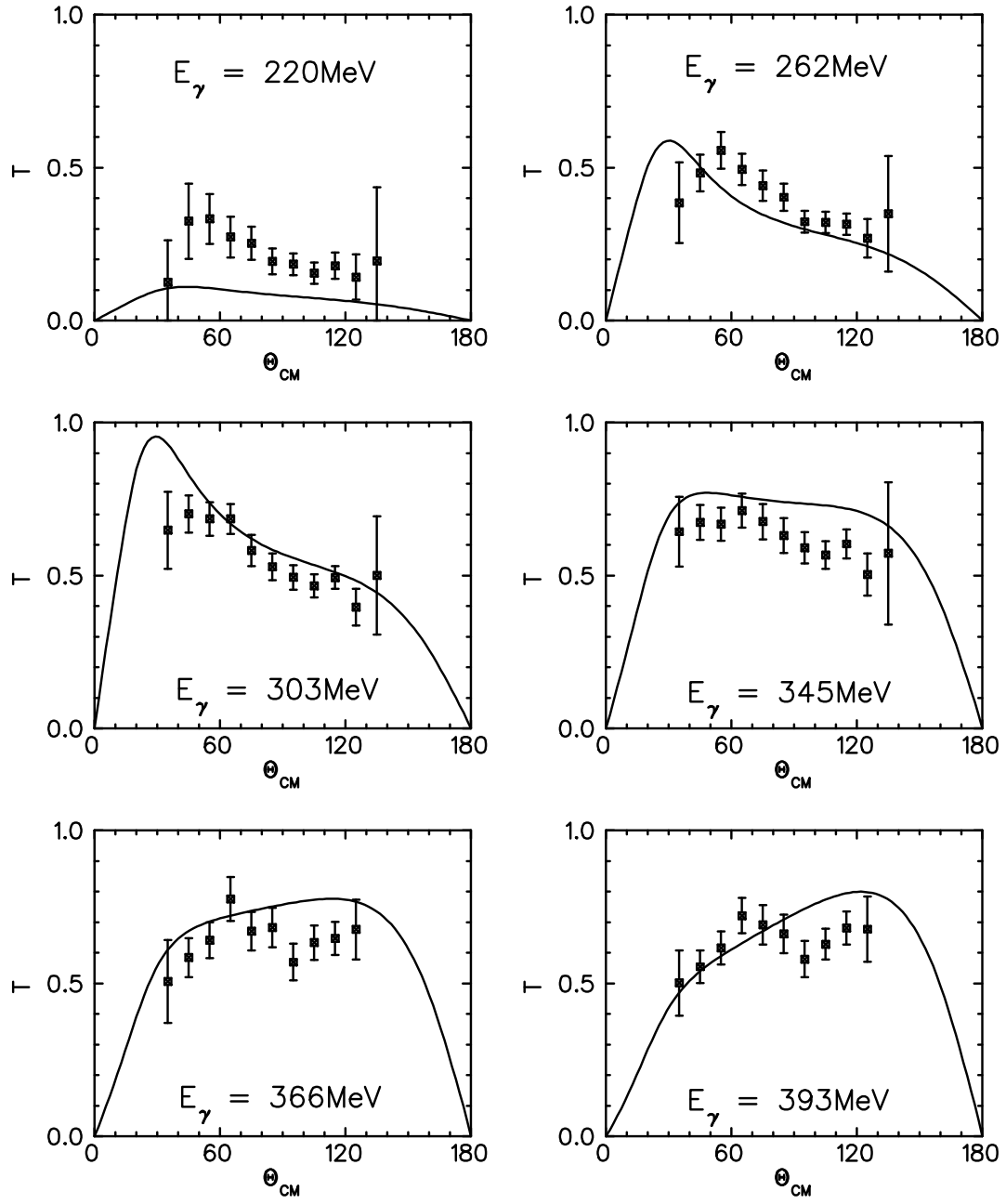


FIG. 5. The target asymmetry T for $\gamma p \rightarrow \pi^+ n$. The data are from Bonn [20].

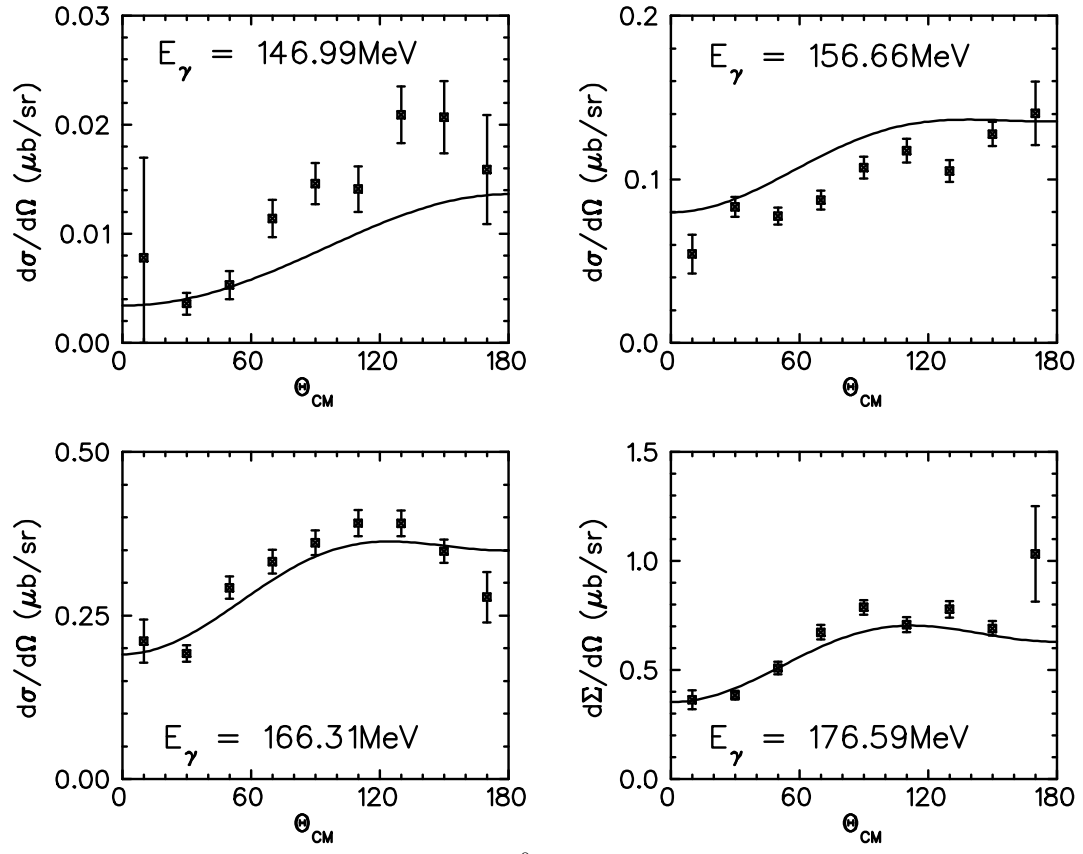


FIG. 6. Differential cross sections for $\gamma p \rightarrow \pi^0 p$ at low energies. The data are from Mainz [15].

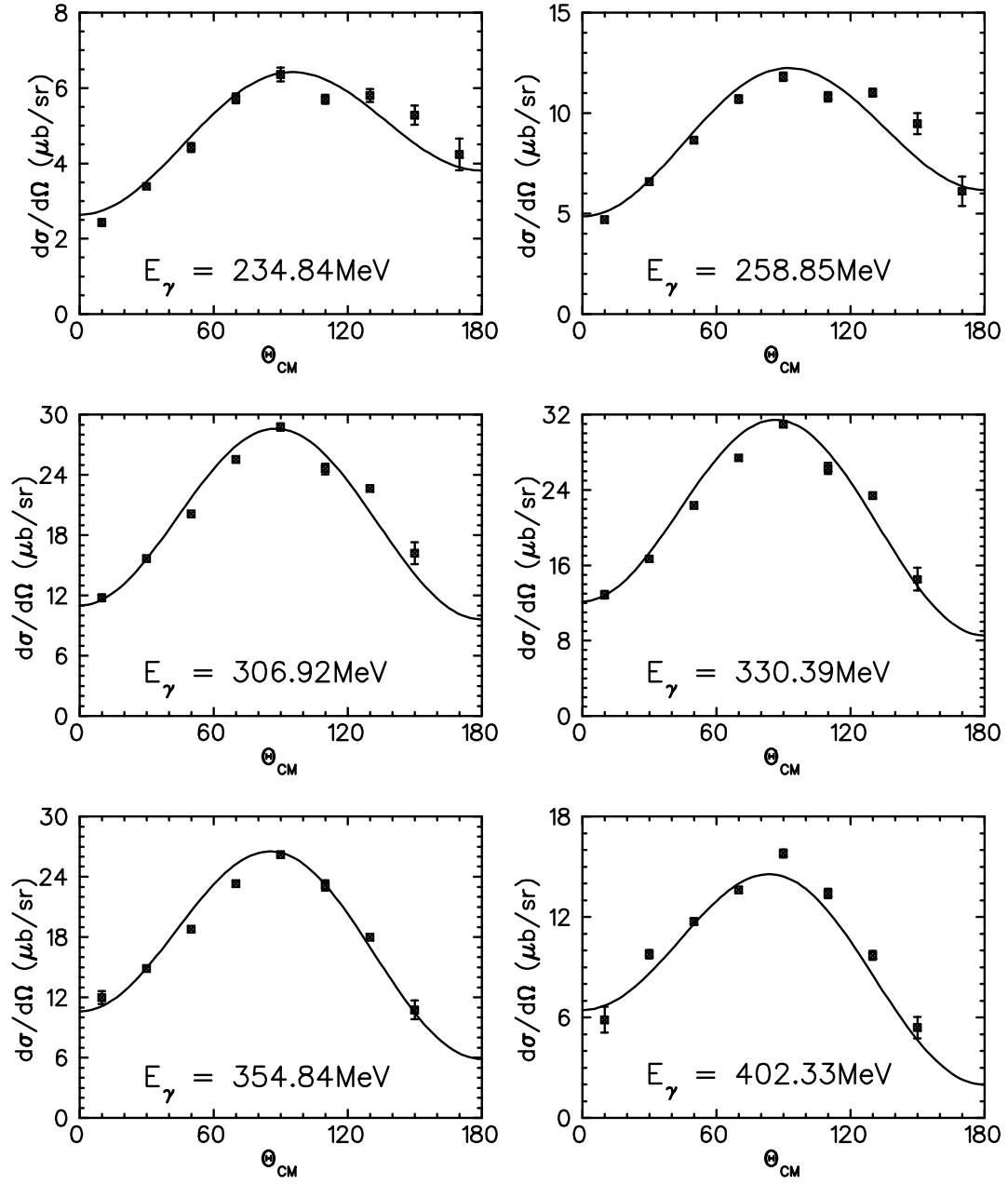


FIG. 7. Differential cross sections for $\gamma p \rightarrow \pi^0 p$. The data are from Mainz [17].

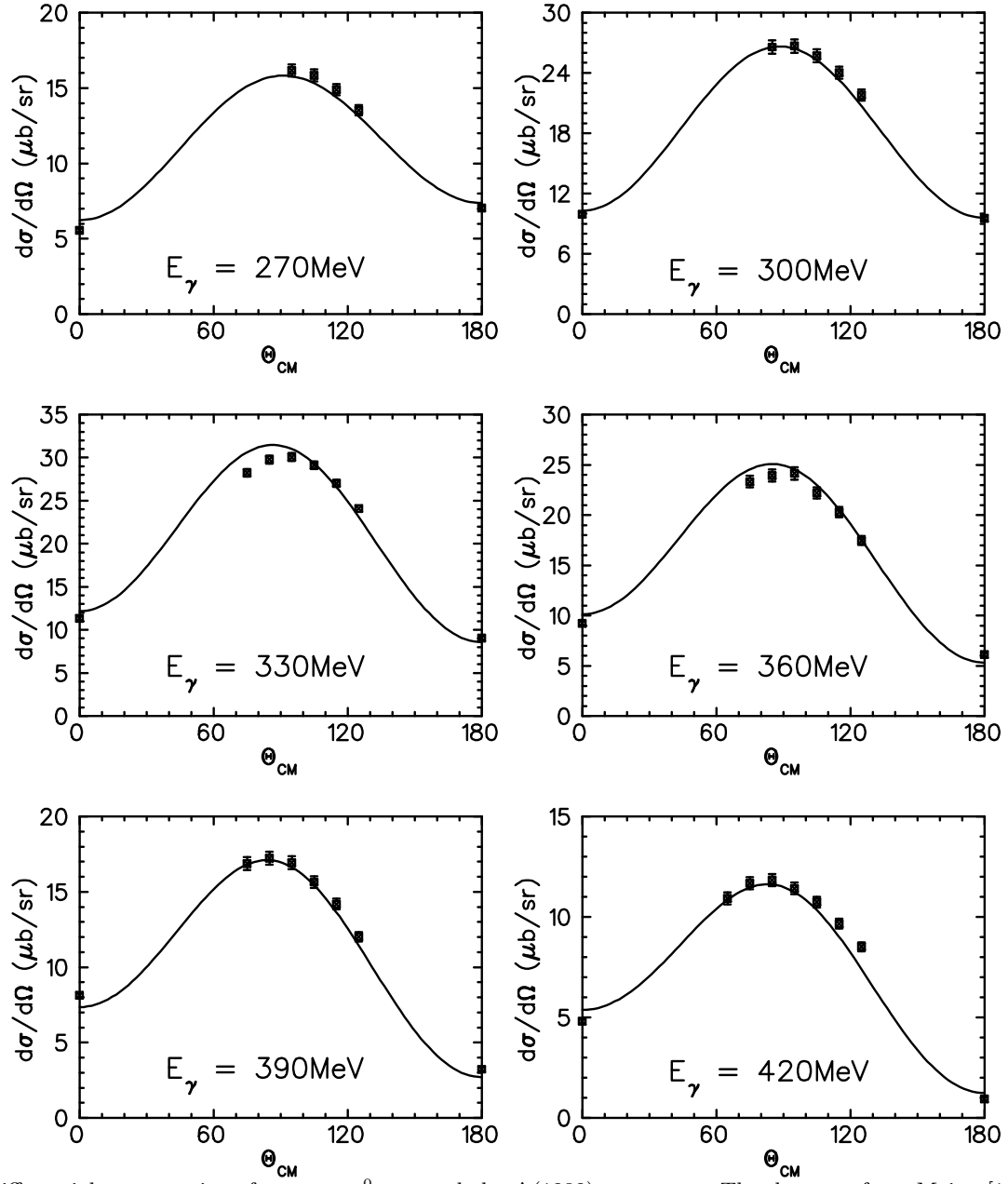


FIG. 8. Differential cross sections for $\gamma p \rightarrow \pi^0 p$ around the $\Delta(1232)$ -resonance. The data are from Mainz [16] except the data at the angles of 0° and 180° which are from Bonn [61].

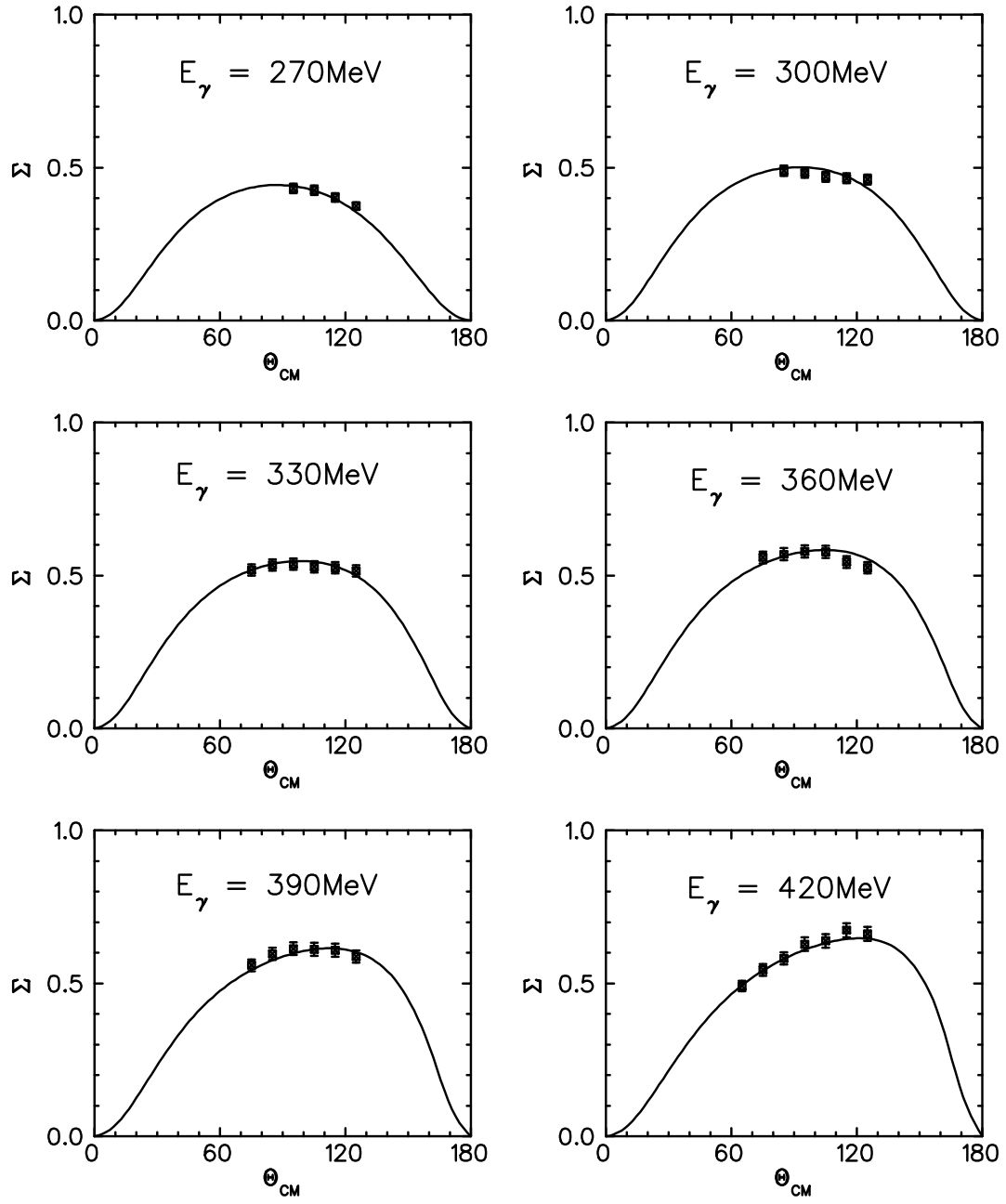


FIG. 9. The beam asymmetry Σ for $\gamma p \rightarrow \pi^0 p$. The data are from Mainz [16].

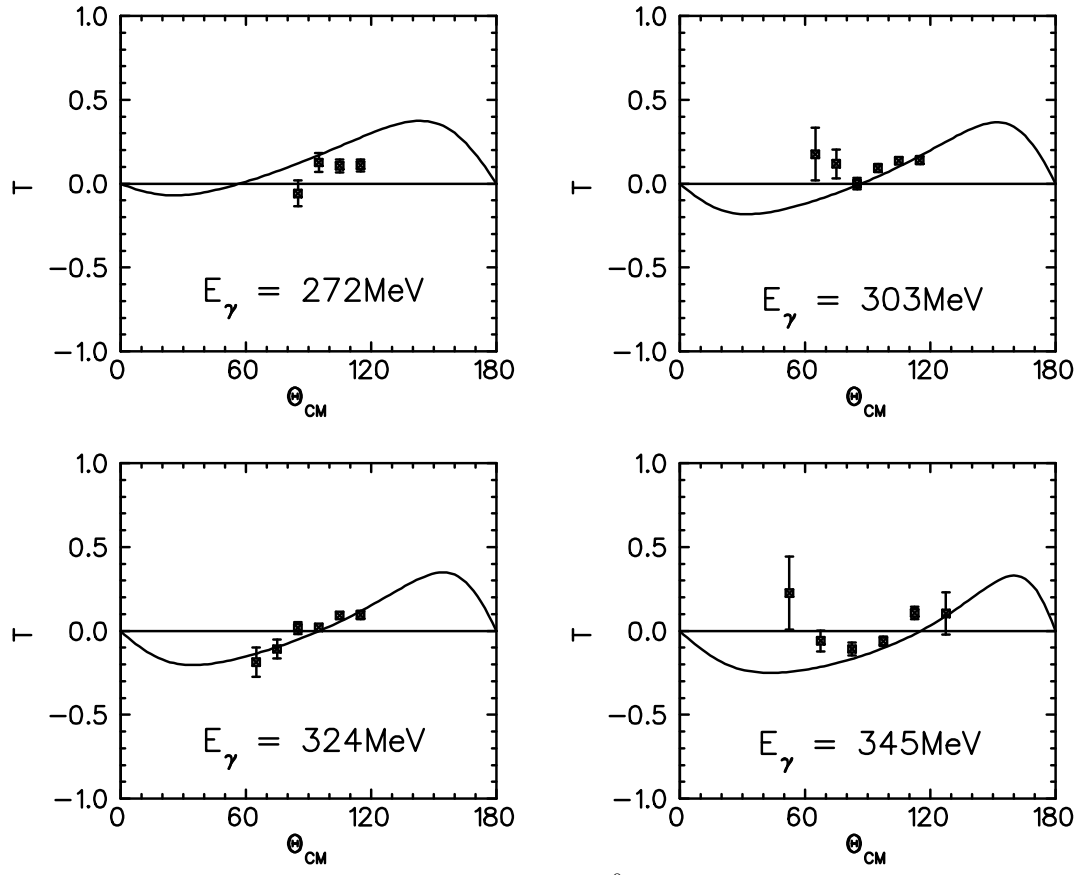


FIG. 10. The target asymmetry T for $\gamma p \rightarrow \pi^0 p$. The data are from Bonn [20].

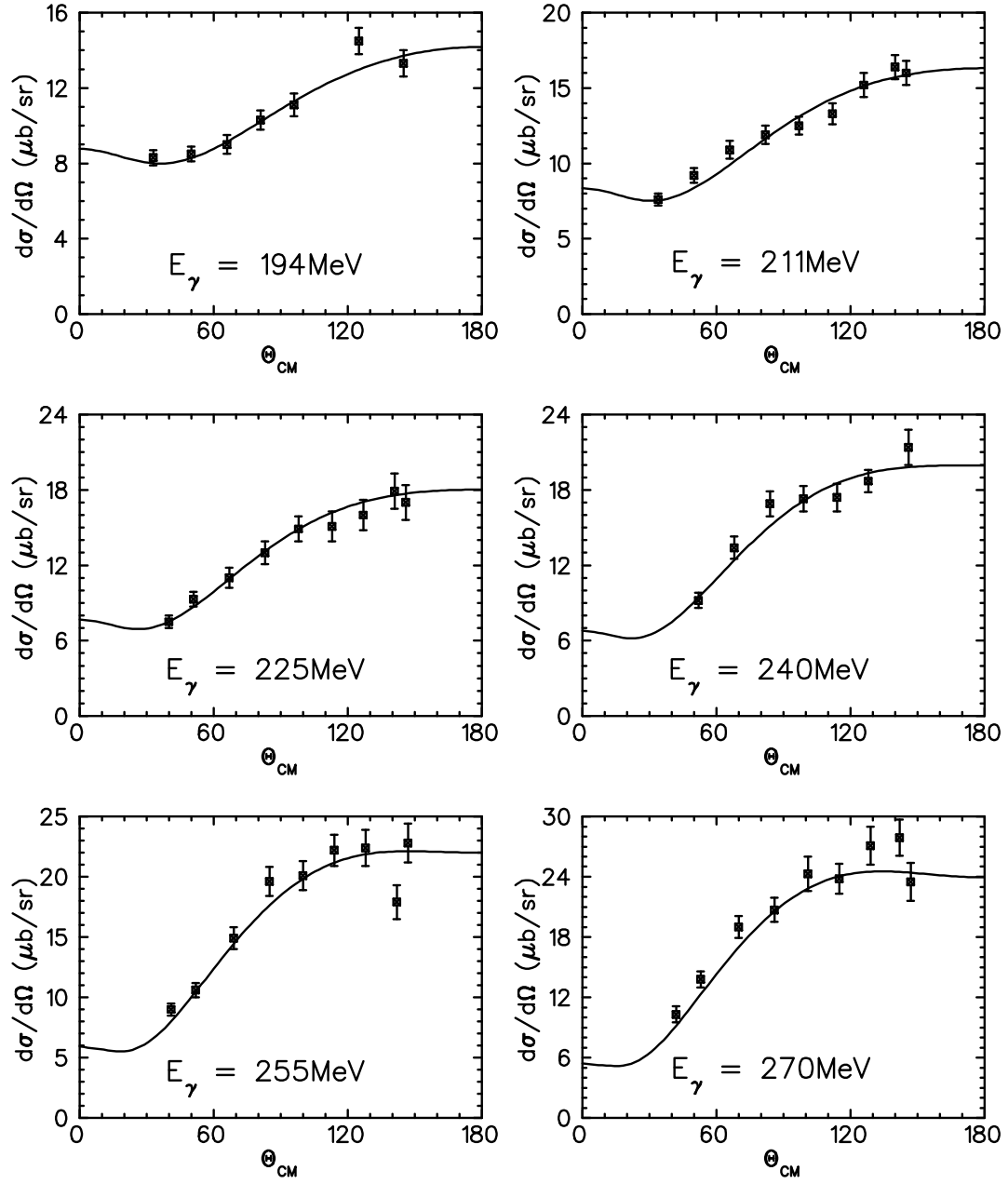


FIG. 11. Differential cross sections for $\gamma n \rightarrow \pi^- p$. The data are from TRIUMF [25].

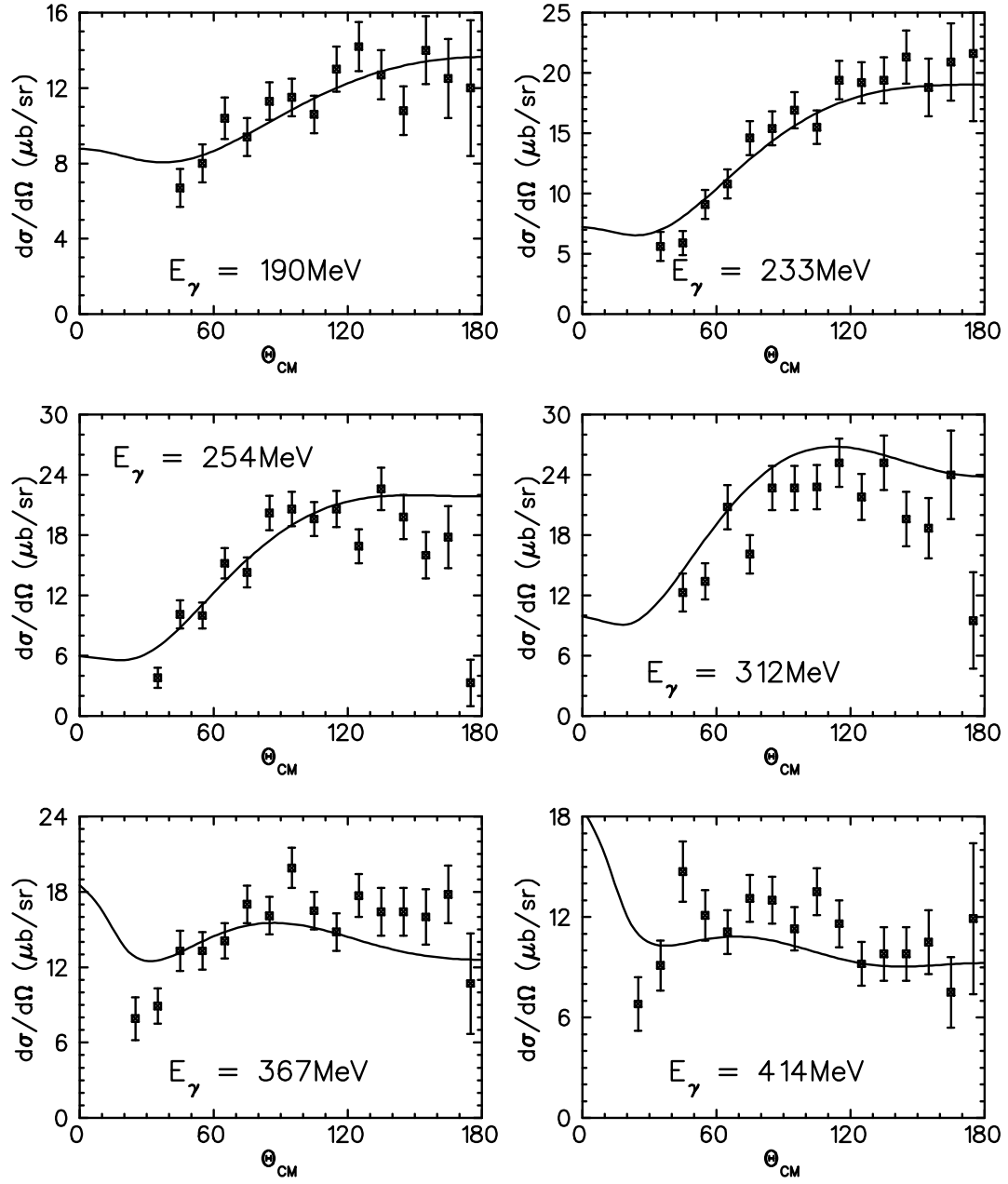


FIG. 12. Differential cross sections for $\gamma n \rightarrow \pi^- p$. The data are from Frascati [22].

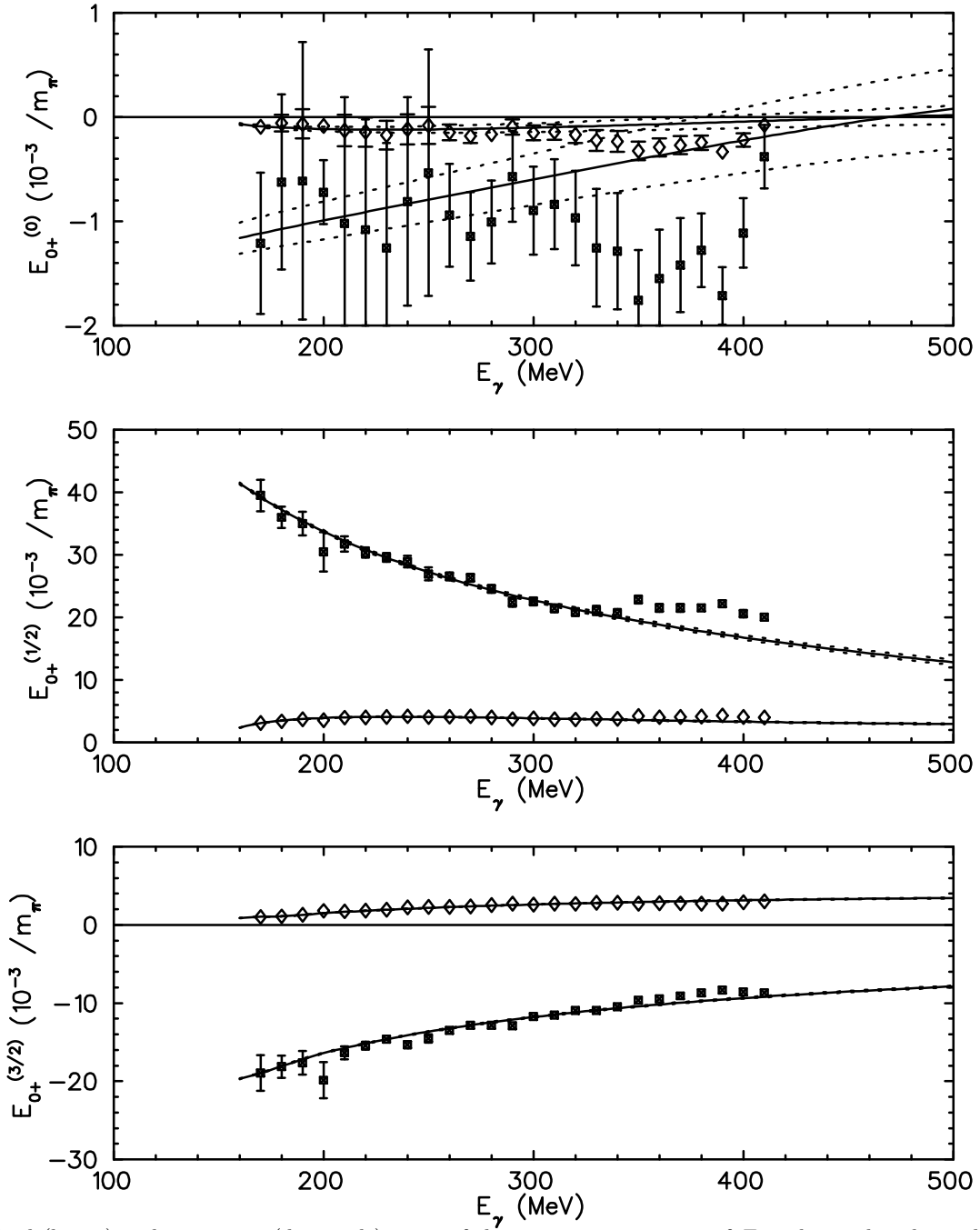


FIG. 13. Real (boxes) and imaginary (diamonds) parts of the isospin components of E_{0+} obtained with our local fit. The solid lines are the corresponding results of the global fit, the dashed lines indicate the error band.

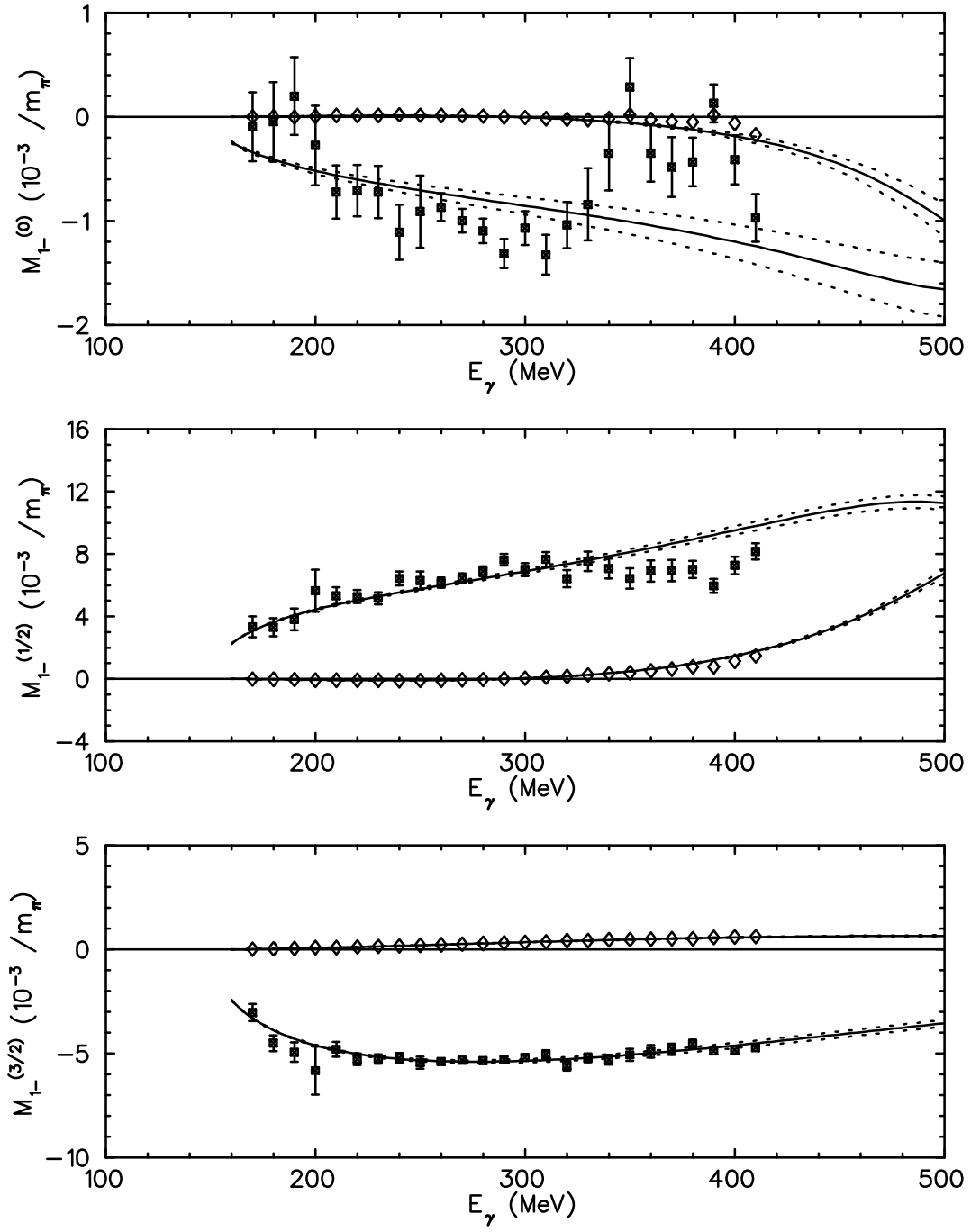


FIG. 14. Isospin components of M_{1-} . Symbols as in Fig. 13.

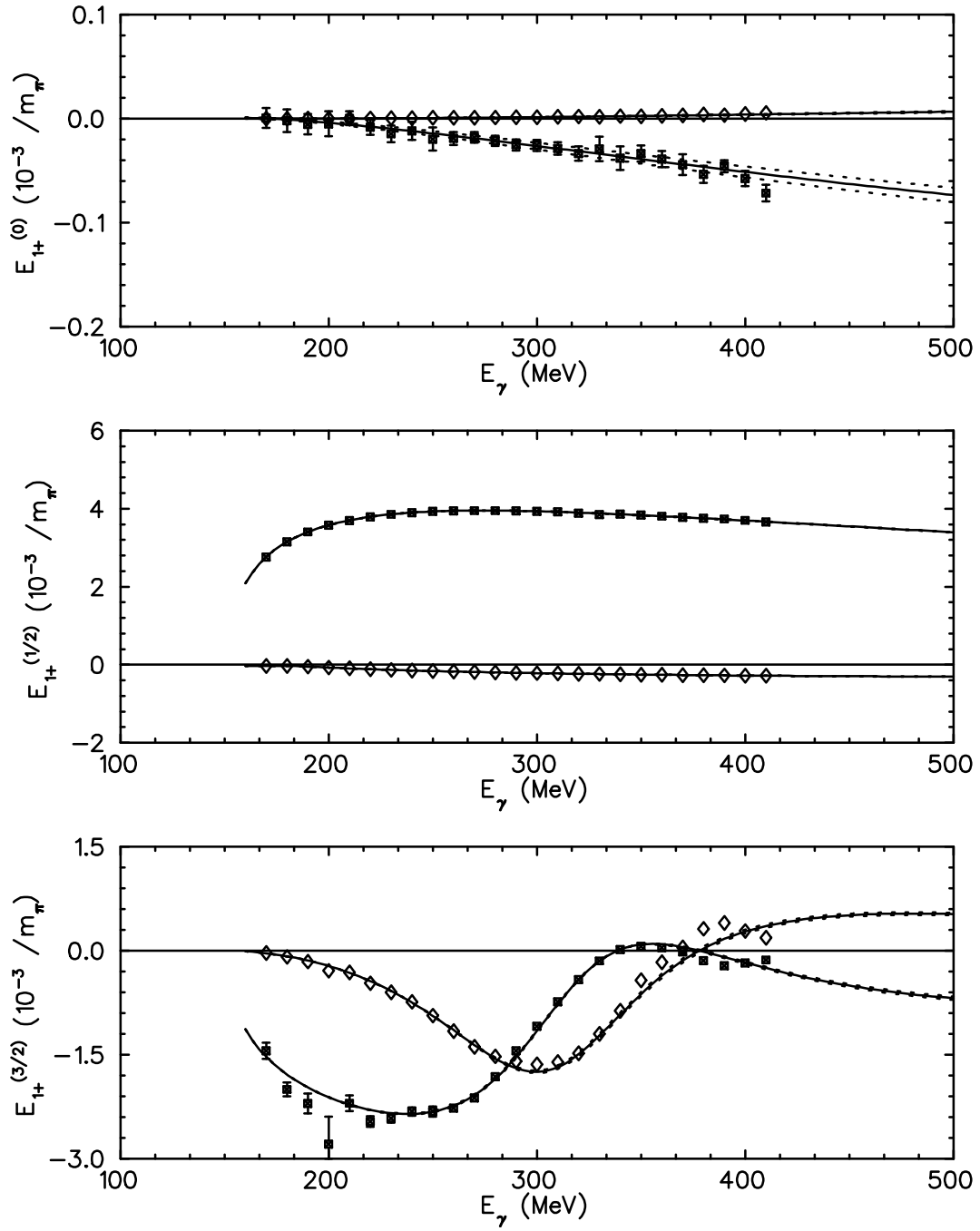


FIG. 15. Isospin components of E_{1+} . Symbols as in Fig. 13.

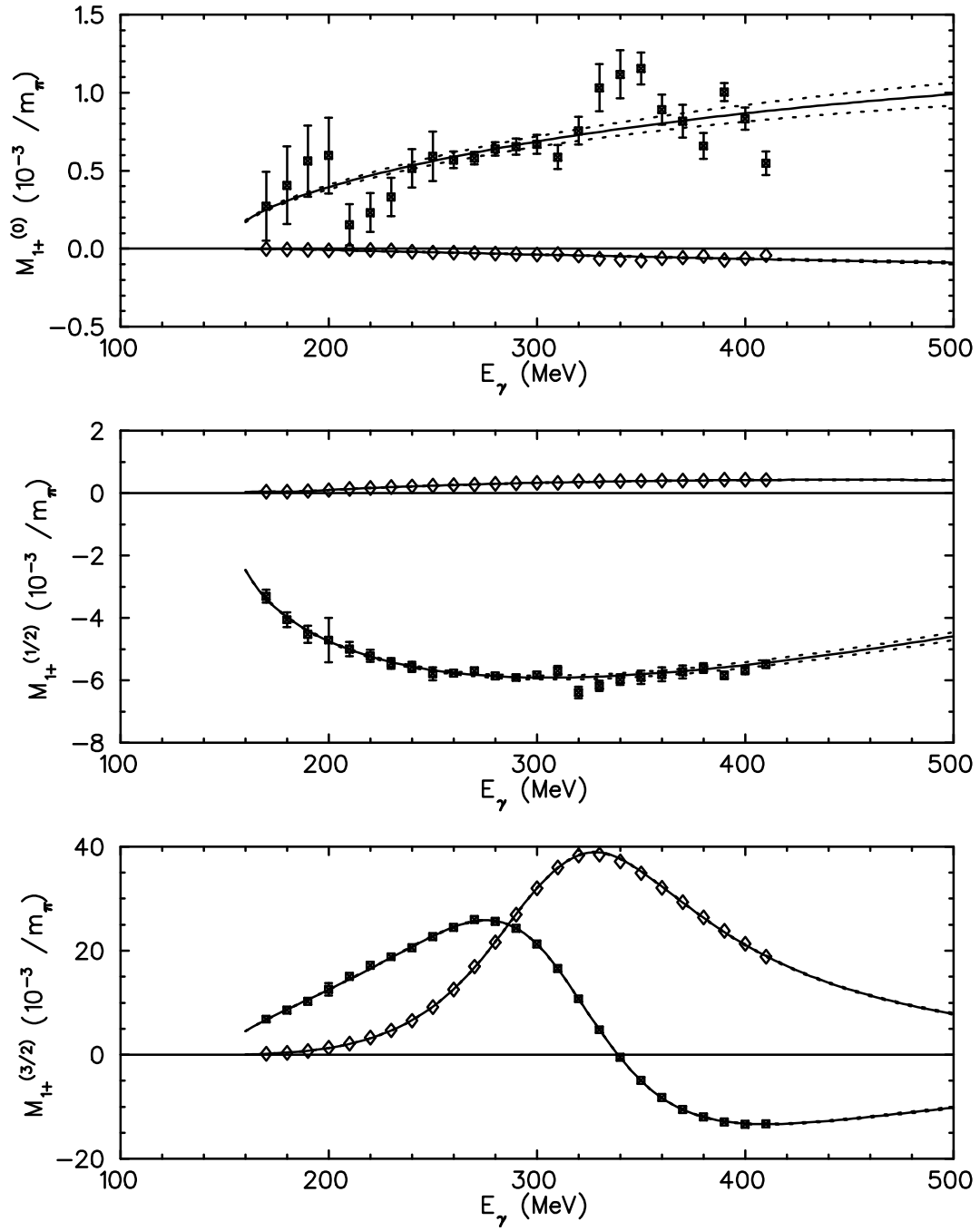


FIG. 16. Isospin components of M_{1+} . Symbols as in Fig. 13.

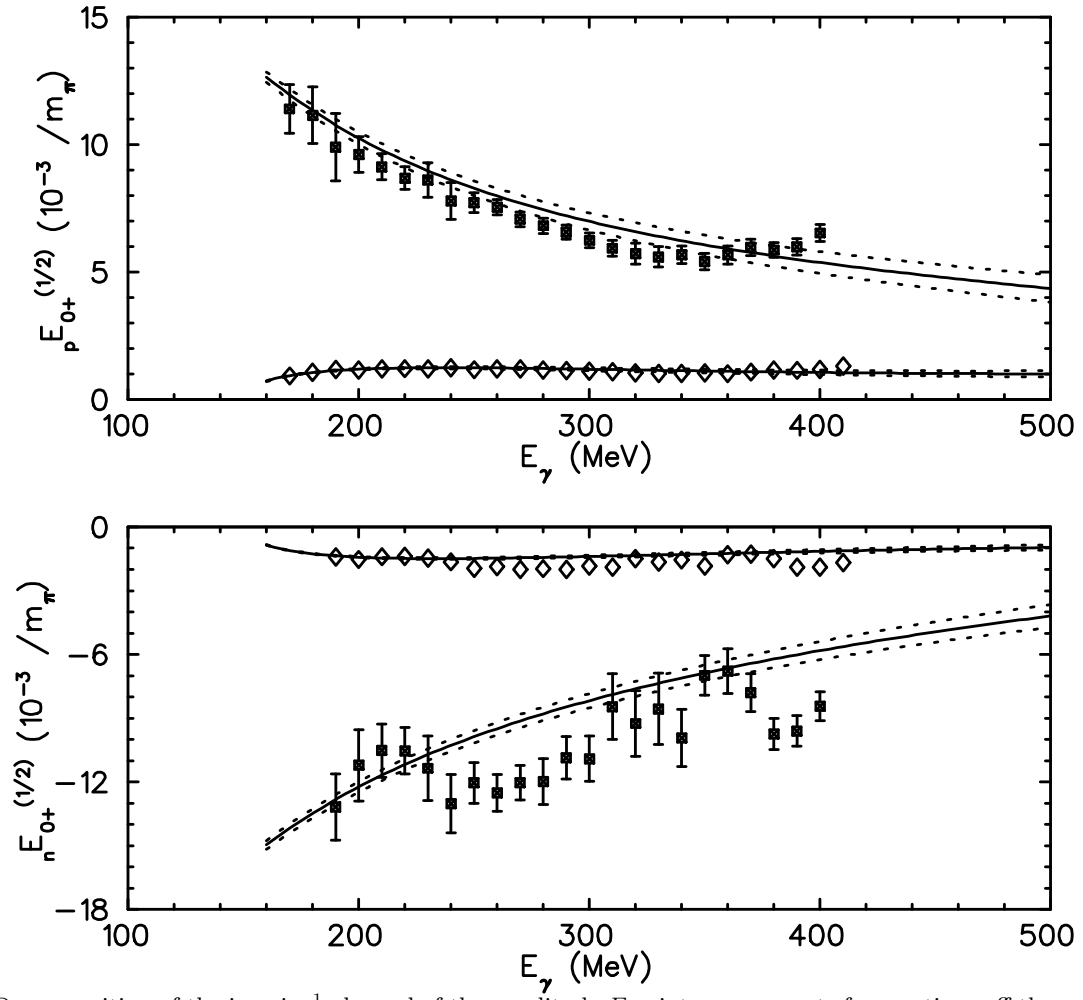


FIG. 17. Decomposition of the isospin $\frac{1}{2}$ channel of the amplitude E_{0+} into components for reactions off the proton and the neutron respectively. Symbols as in Fig. 13.

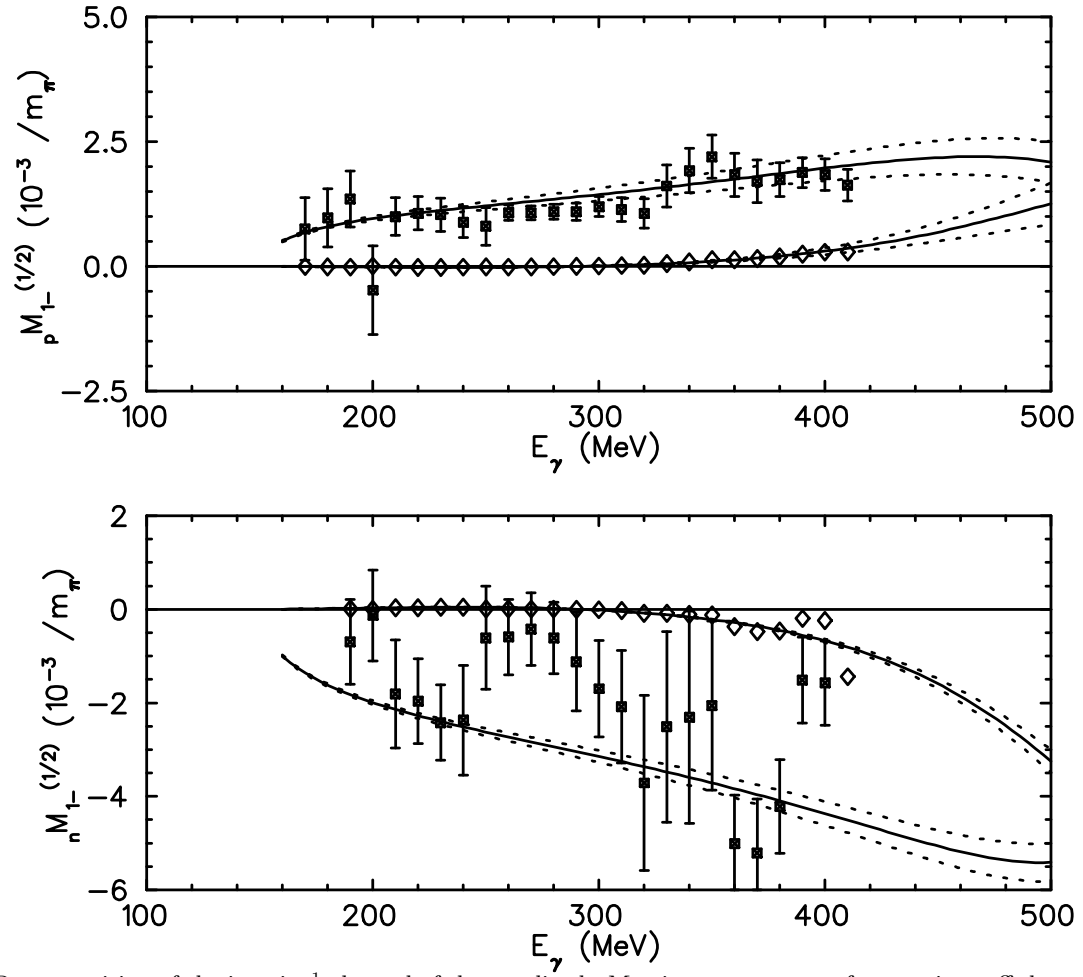


FIG. 18. Decomposition of the isospin $\frac{1}{2}$ channel of the amplitude M_{1-} into components for reactions off the proton and the neutron respectively. Symbols as in Fig. 13.

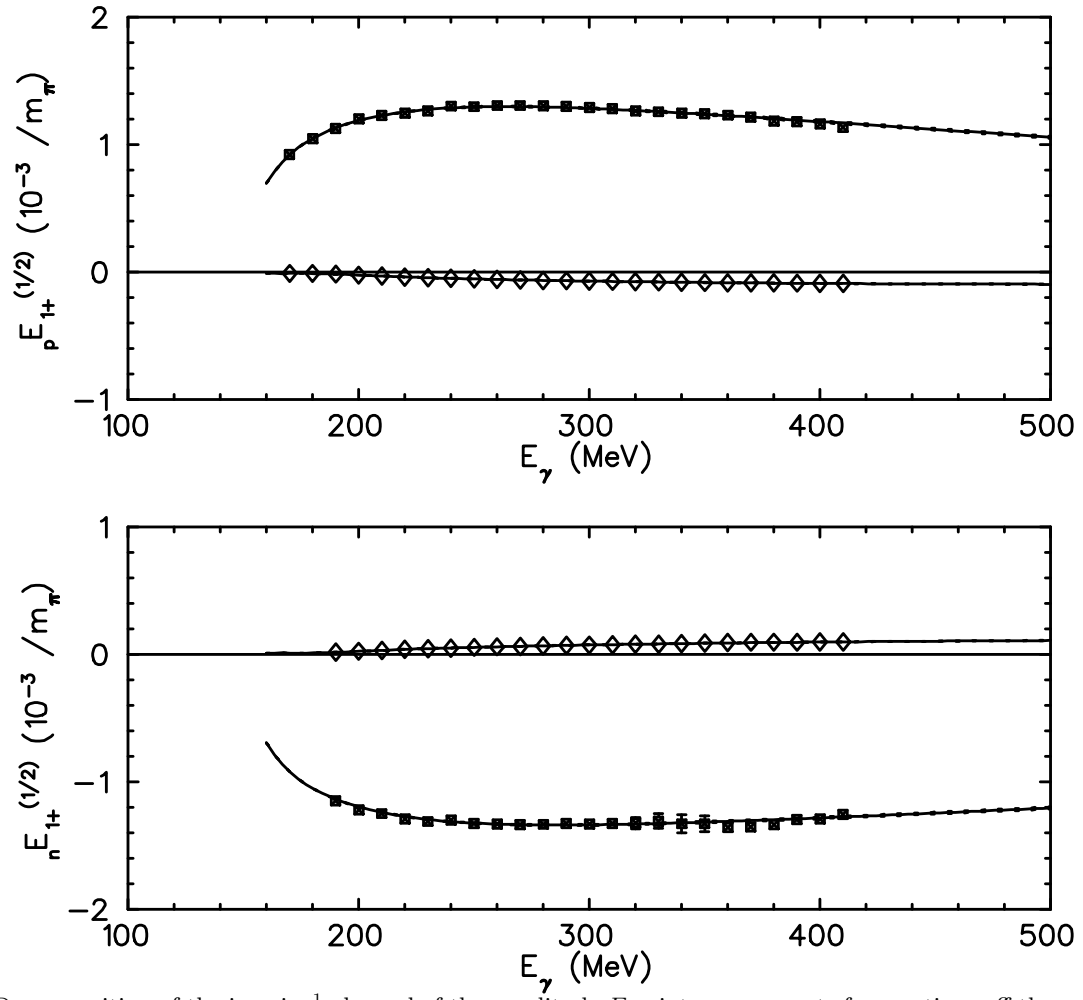


FIG. 19. Decomposition of the isospin $\frac{1}{2}$ channel of the amplitude E_{1+} into components for reactions off the proton and the neutron respectively. Symbols as in Fig. 13.

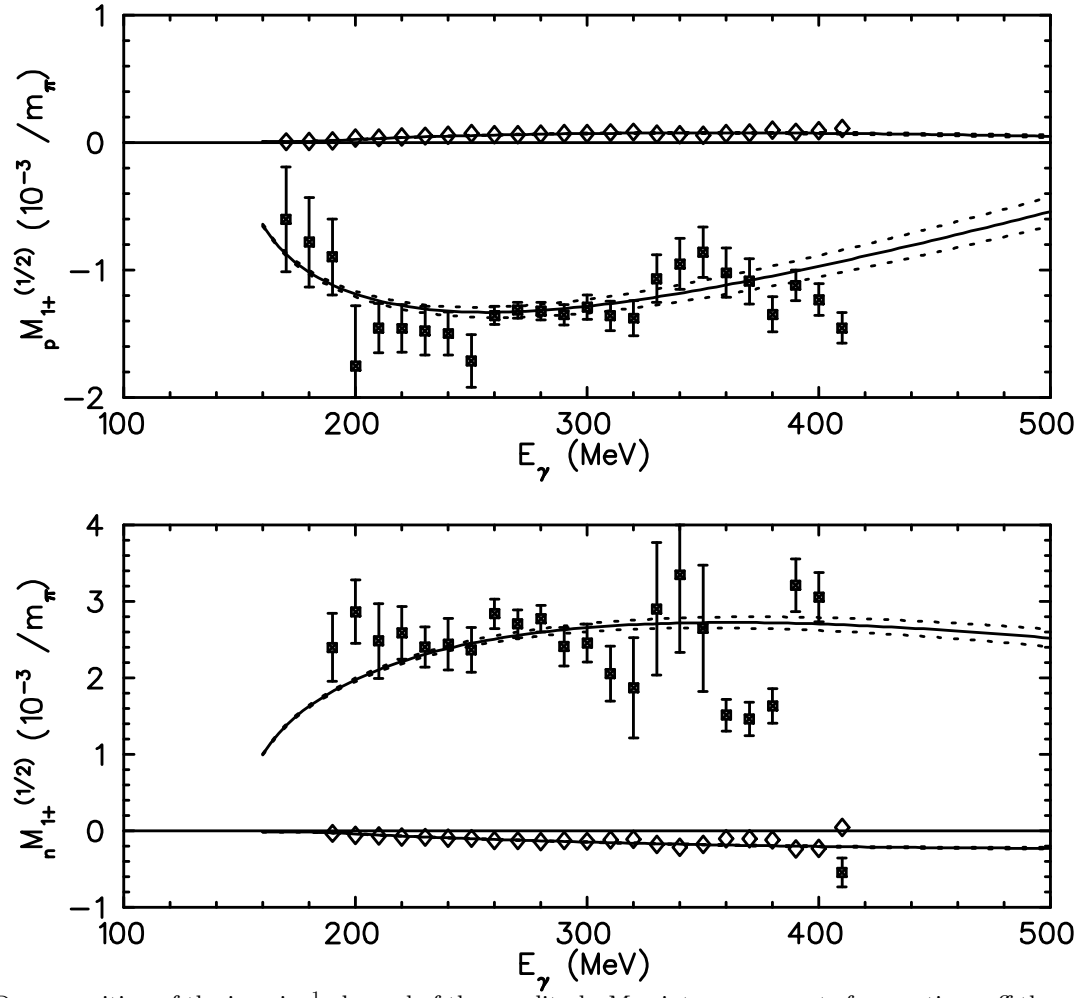


FIG. 20. Decomposition of the isospin $\frac{1}{2}$ channel of the amplitude M_{1+} into components for reactions off the proton and the neutron respectively. Symbols as in Fig. 13.

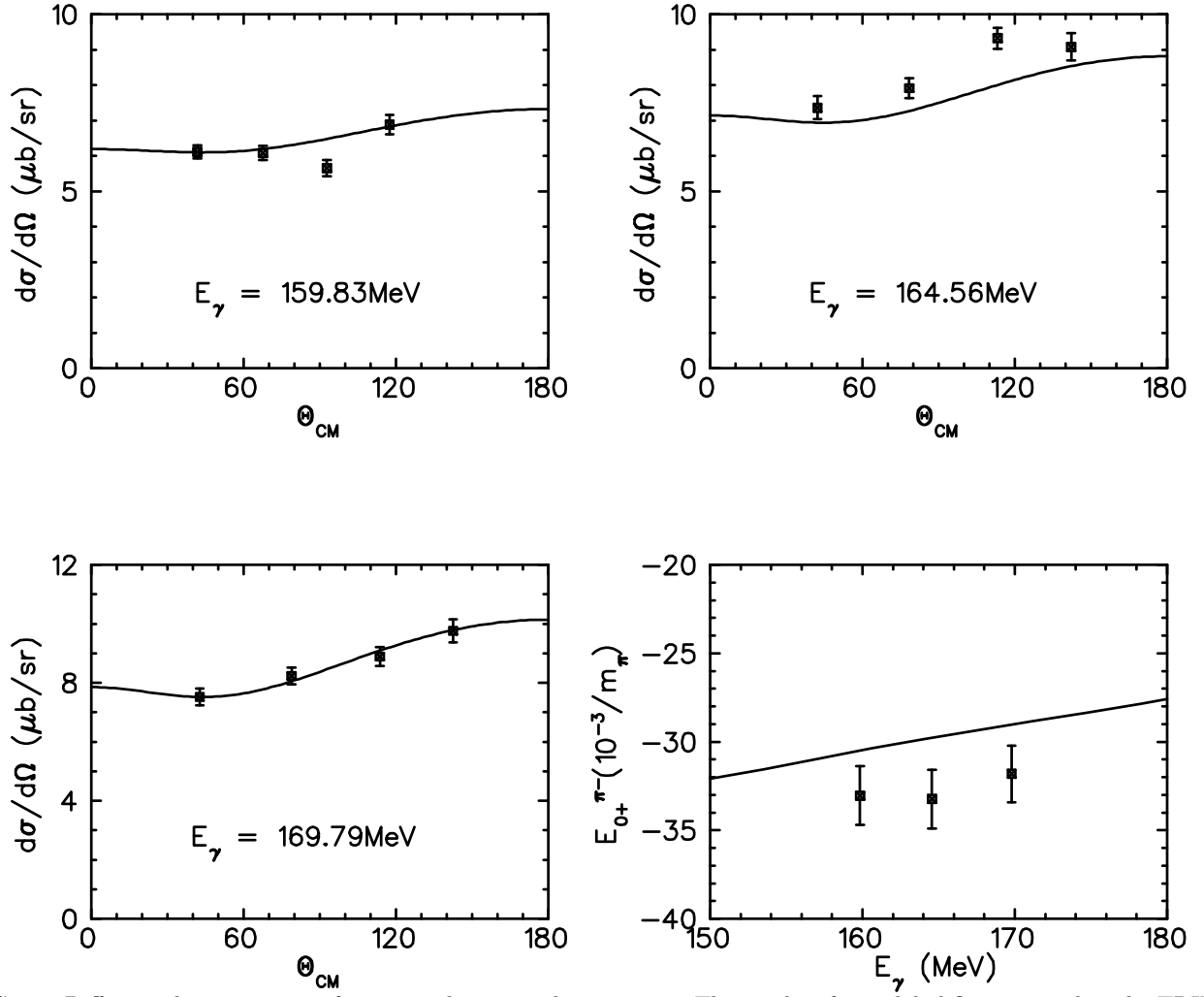


FIG. 21. Differential cross sections for π^- production at low energies. The results of our global fit compared to the TRIUMF data [30] for $\gamma n \rightarrow \pi^- p$. The data points for E_{0+} are also from Ref. [30].

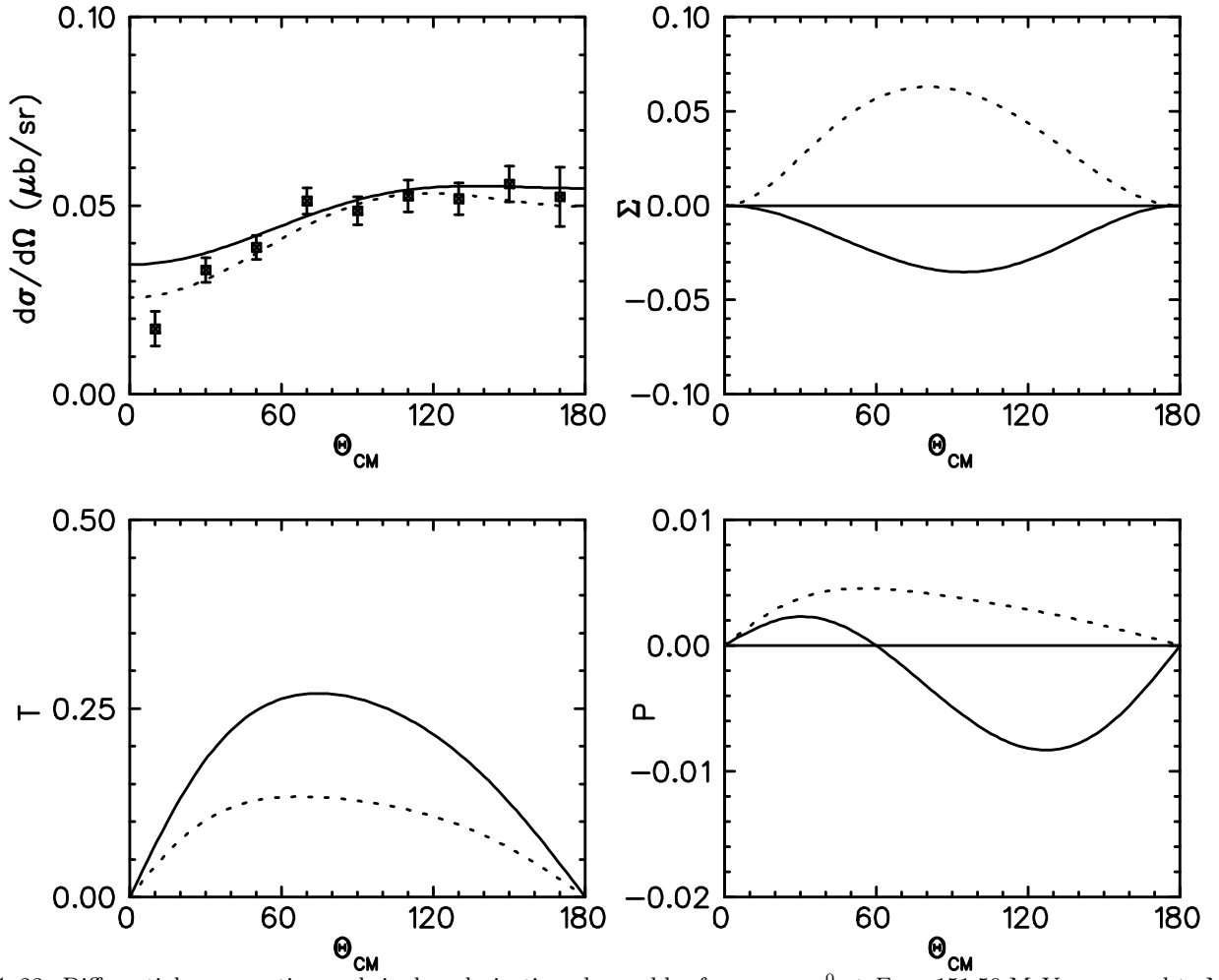


FIG. 22. Differential cross section and single polarization observables for $\gamma p \rightarrow p\pi^0$ at $E_\gamma = 151.59$ MeV compared to Mainz data [15]. The dotted line is obtained by reducing the contribution of the M_{1-} amplitude by 20 % (see text).

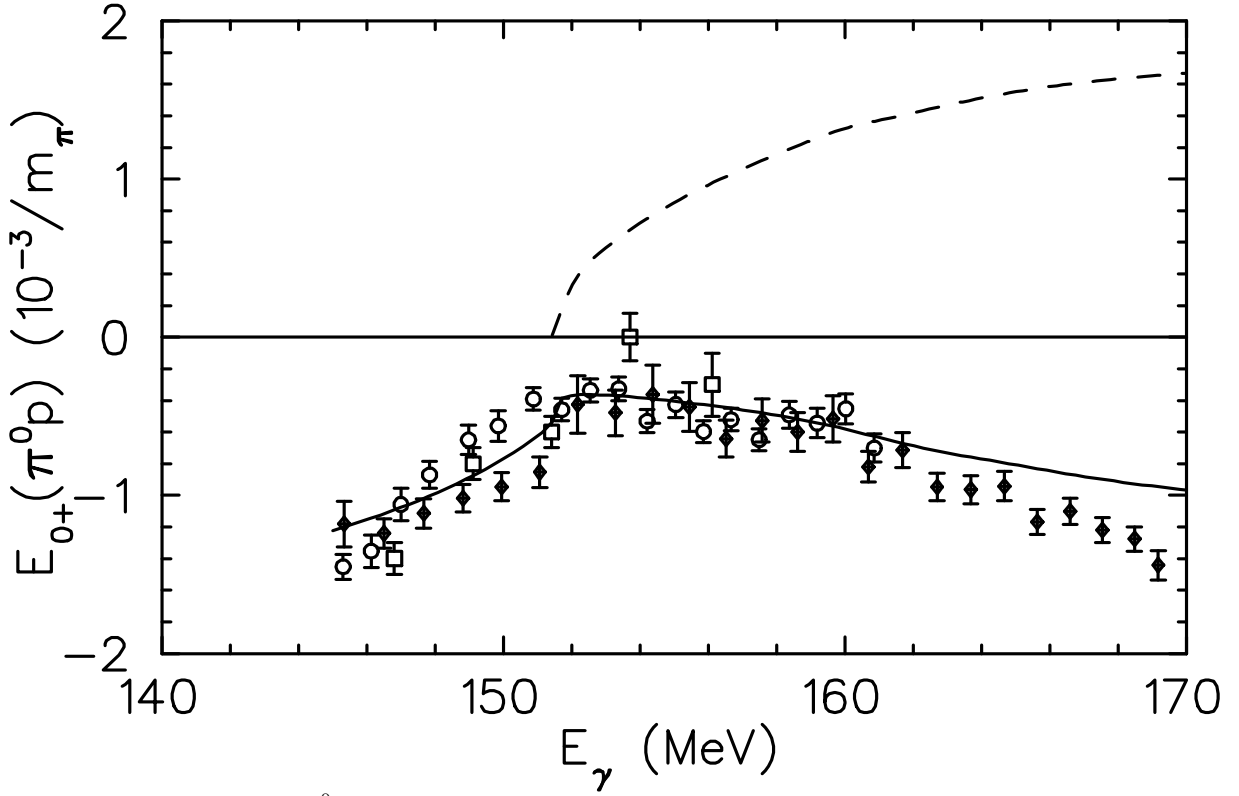


FIG. 23. The amplitude $E_{0+}(p\pi^0)$ in comparison with the recent analyses of data from Mainz [15,62], open circles, and Saskatoon [35], diamonds. The open squares are the result of an analysis of an earlier experiment at Mainz [34,7]. The dashed line shows our prediction for $\text{Im}E_{0+}$, the solid line for $\text{Re}E_{0+}$ respectively. The unitarity parameter β discussed in [62] describes the rise of $\text{Im}E_{0+}$ at π^+ threshold via $\text{Im}E_{0+} = i\beta q_+$. In our calculation $\beta = 4.3$, to be compared with the values 3.76 ± 0.11 corresponding to the unitary fit of Ref. [62] and the ChPT value 2.78 [63], all in units of $10^{-3}/m_{\pi^+}^2$.

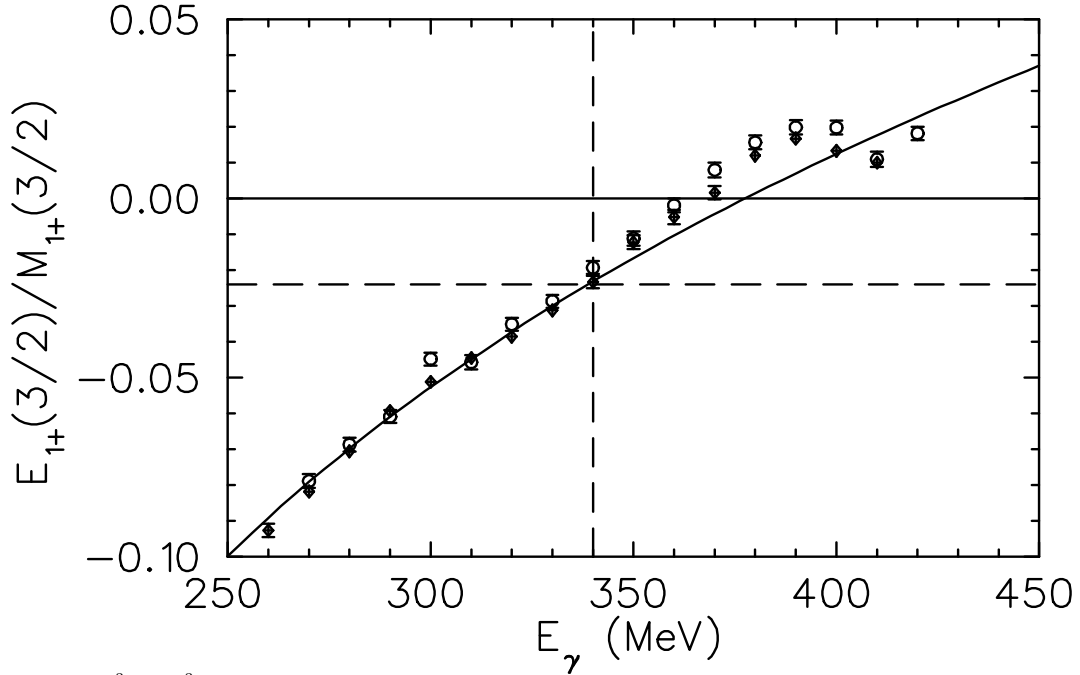


FIG. 24. The ratio $E_{1+}^{(3/2)}/M_{1+}^{(3/2)}$ as a function of E_γ . Solid line: global fit, diamonds: local fit, circles: analysis of Krahn [16].

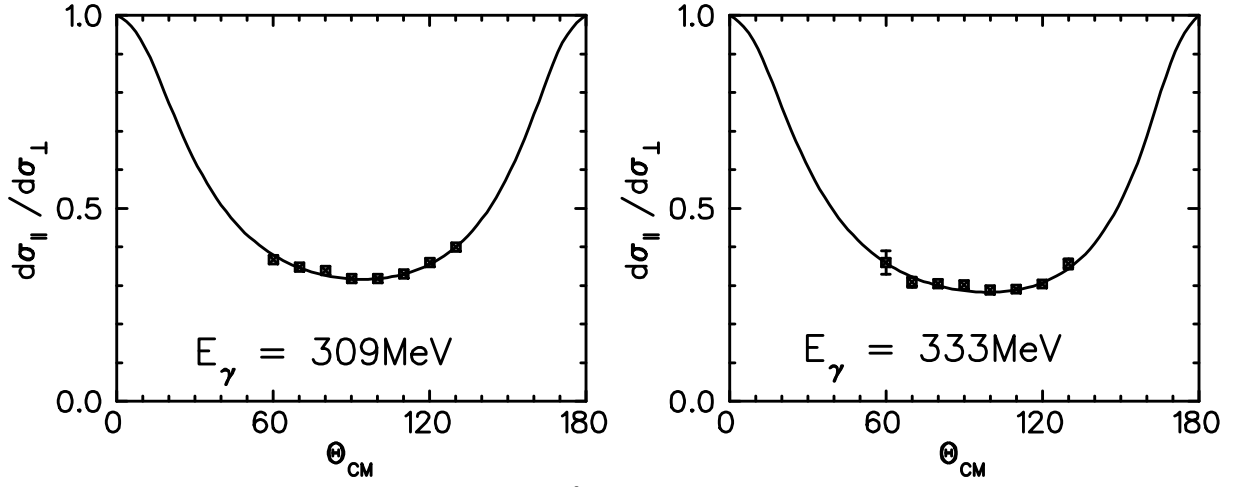


FIG. 25. The ratio $d\sigma_{||}/d\sigma_{\perp}$ for $\gamma p \rightarrow p\pi^0$ compared to the analysis of Sandorfi et al. [48].

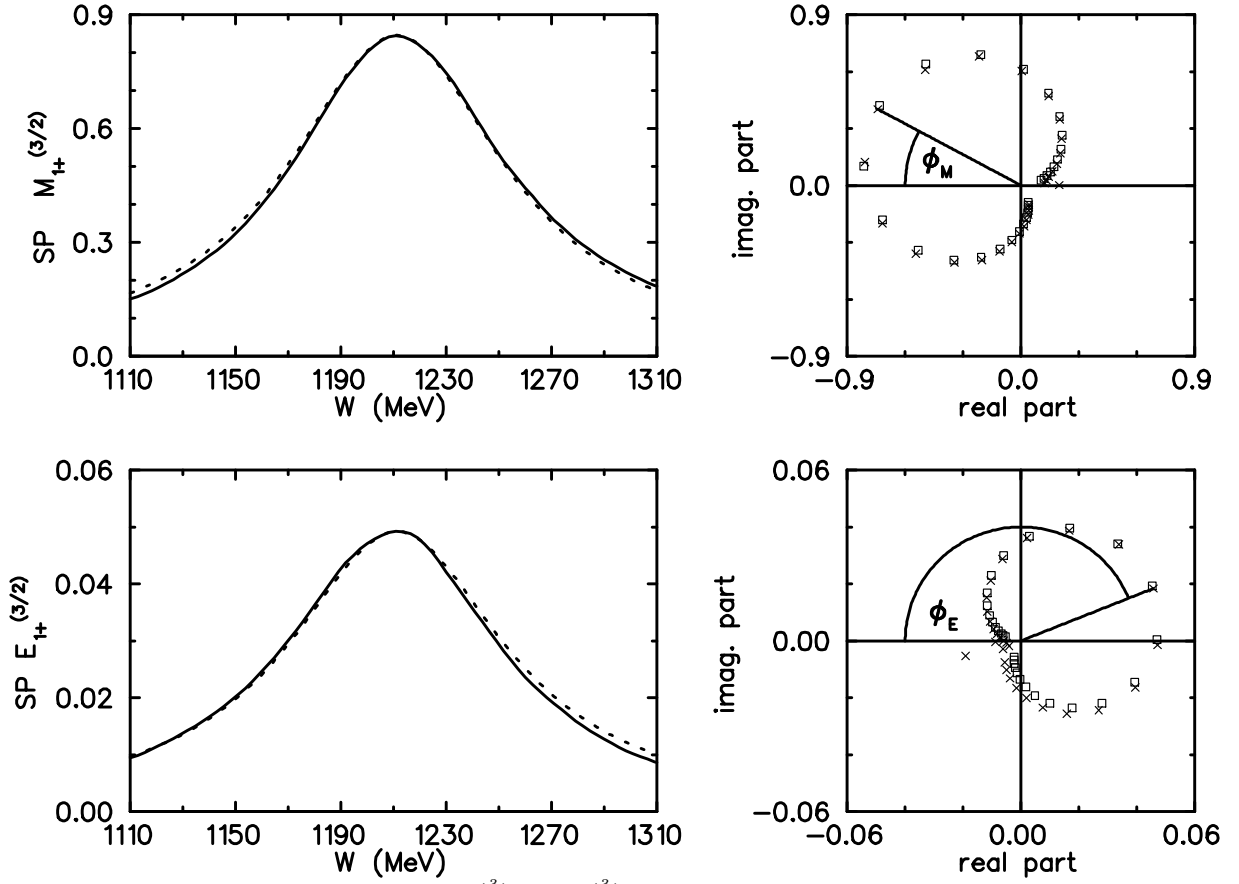


FIG. 26. Left: The speed of the multipoles $M_{1+}^{(3/2)}$ and $E_{1+}^{(3/2)}$ (solid line) compared to the case of an ideal resonance pole (dotted line). Right: The speed vectors for these multipoles in the complex plane (crosses) compared to the case of an ideal resonance pole (squares).

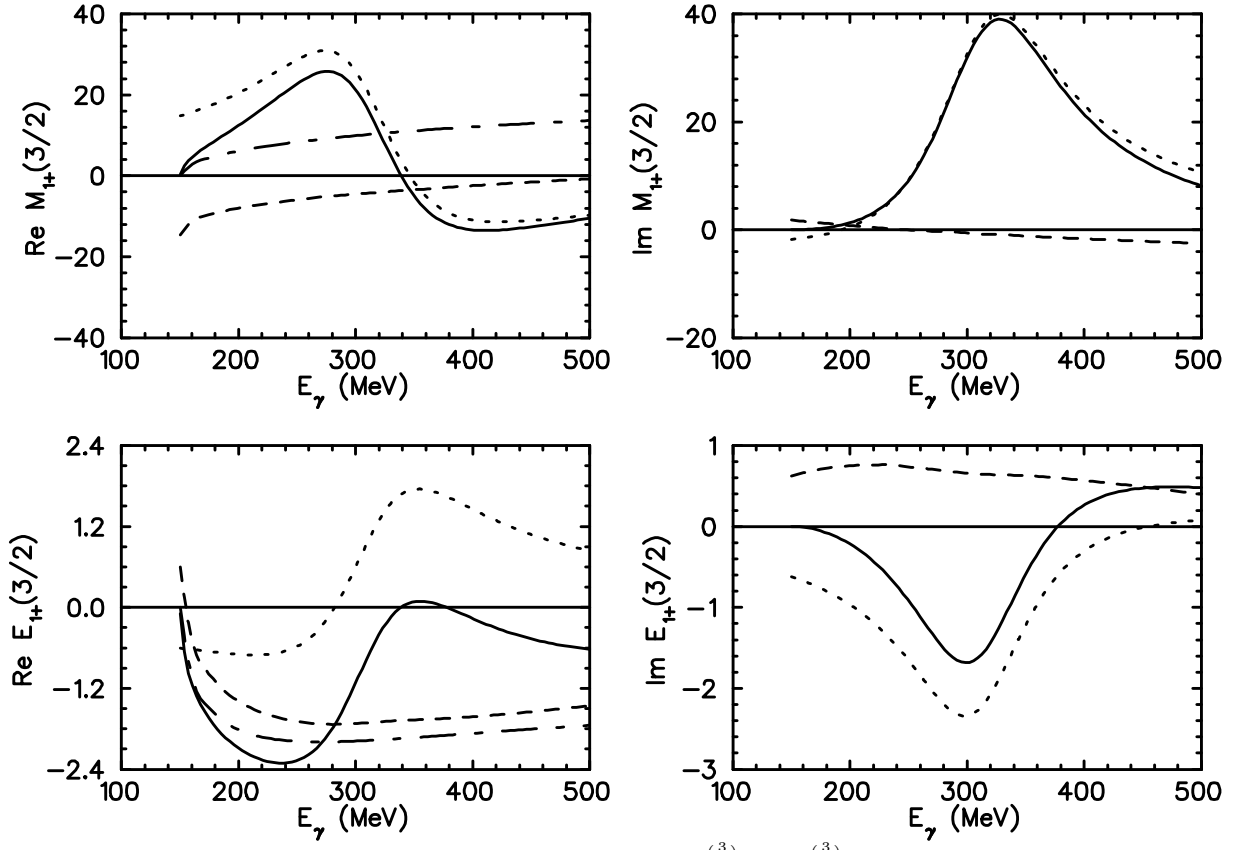


FIG. 27. Separation of resonance and background contributions for $M_{1+}^{(3/2)}$ and $E_{1+}^{(3/2)}$ into full amplitude (solid lines), resonance pole (dotted lines), background (dashed lines) and Born terms only (dashed-dotted lines).

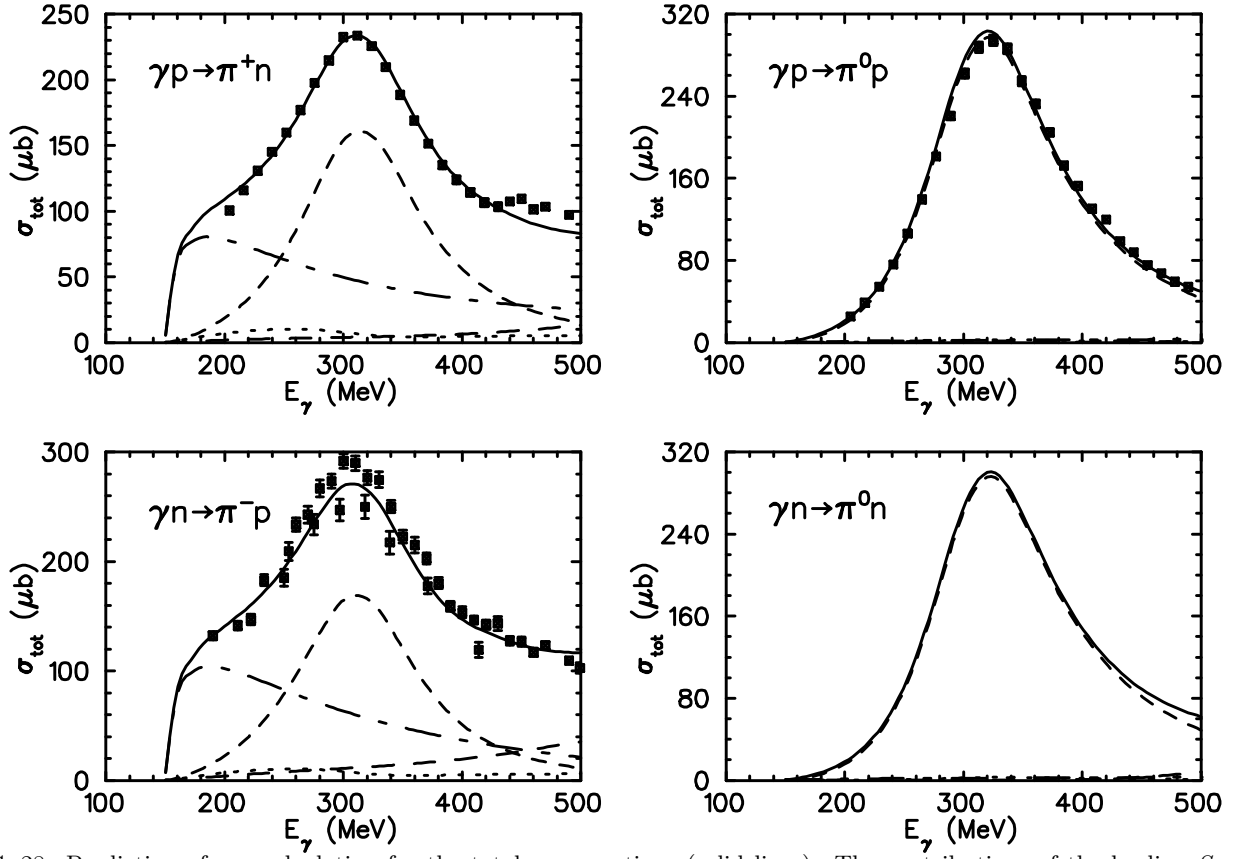


FIG. 28. Prediction of our calculation for the total cross sections (solid lines). The contributions of the leading S and P wave multipoles are also shown: M_{1+} (dashed lines), E_{0+} (dashed-dotted lines), M_{1-} (long dashed lines), E_{1+} (dotted lines). The data are from Mainz [17,64] for π^+ and π^0 , and from Tokyo [65] and Frascati [66] for π^- .

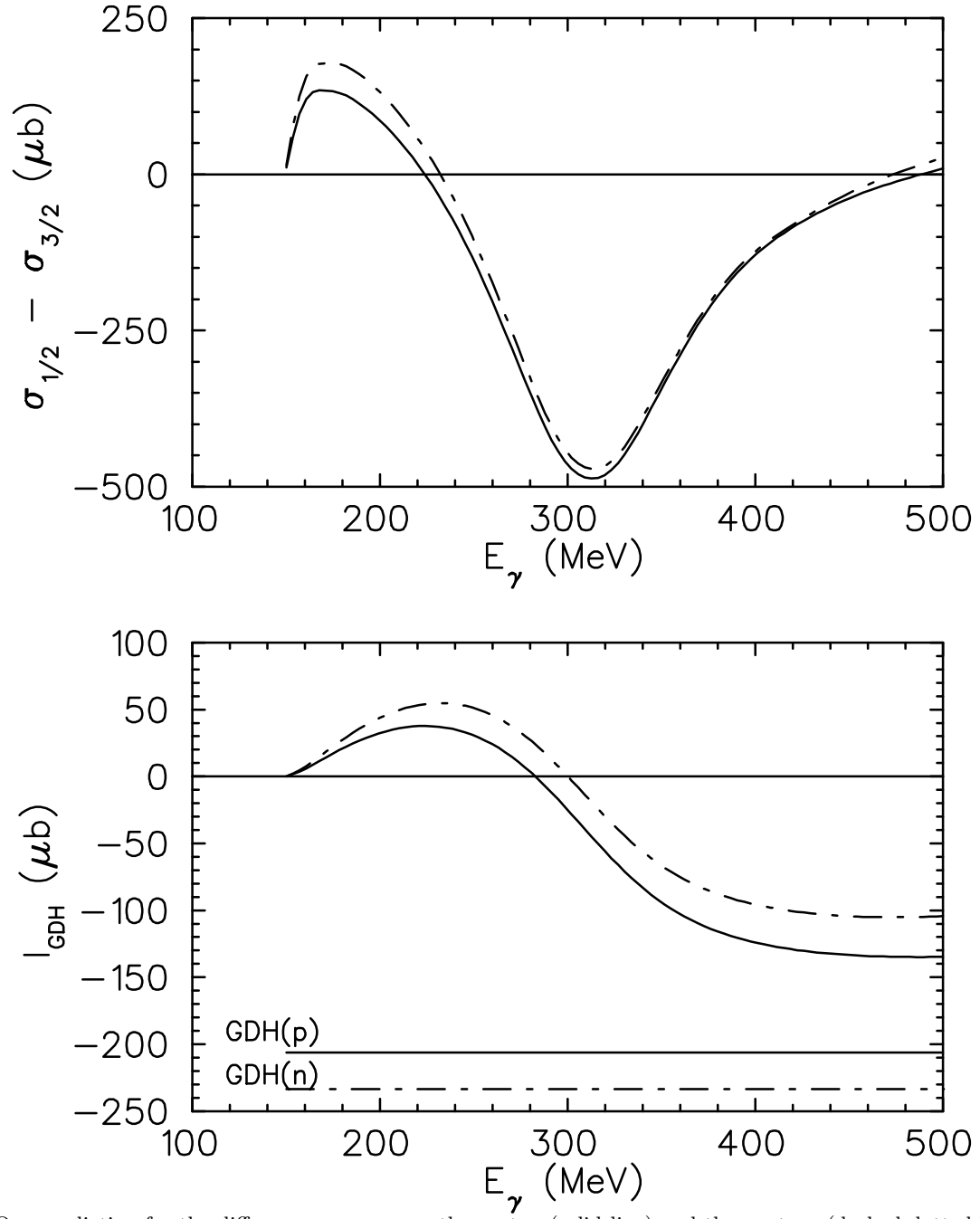


FIG. 29. Our prediction for the difference $\sigma_{1/2} - \sigma_{3/2}$ on the proton (solid line) and the neutron (dashed-dotted line) and the corresponding contributions to the GDH integral, which are evaluated as functions of the upper limit of integration. We also indicate the predictions of the sum rule.